TECHNISCHE UNIVERSITÄT WIEN

ATOMINSTITUT

DIPLOMA THESIS

Towards the fabrication of fiber-based Fabry Perot Cavities

for obtaining the academic degree

Diplom-Ingenieur

in the course of studies

Technical Physics

submitted by

Constantin Grave, BSc

prepared at the
Institute of Atomic and Subatomic Physics,
Faculty of Physics,
TU Wien

supervised by
Assistant Prof. Dr. Julian Léonard
Dr. Marvin Holten

Vienna, 15.05.2024

TECHNISCHE UNIVERSITÄT WIEN

ATOMINSTITUT

DIPLOMARBEIT

Vorbereitungen zur Fabrikation von faserbasierten Fabry-Perot-Resonatoren

zur Erlangung des akademischen Grades

Diplom-Ingenieur

im Rahmen des Studiums

Technische Physik

eingereicht von

Constantin Grave, BSc
Matrikelnummer 00271376

ausgeführt am Atominstitut
der Fakultät für Physik
der Technischen Universität Wien

Betreuung
Assistant Prof. Dr. Julian Léonard
Dr. Marvin Holten

Wien, 15.05.2024

(Unterschrift Verfasser:in) (Unterschrift Betreuer:in)

Abstract

To enhance our knowledge and to experimentally access broader realms of physics, further miniaturization of devices seems inevitably. Fabry-Perot interferometers (FPIs), which typically consist of two parallel mirrors that act as a spectral filter, represent the classical optical instruments with the highest spectral resolution before the invention of laser spectroscopy and have stimulated many experiments. The recent progress in the treatment of end-facets of optical fibers has enabled the fabrication of Fiber Fabry Perot cavities (FFPCs), compact devices with small mode volumes, open geometries and high finesses. They can be used in many fields including sensing, nonlinear optics and cavity quantum electrodynamics (CQED). In this thesis, we present a highly automated manufacturing process to fabricate FFPCs with high finesses and customizable geometry. While the shapes of the mirrors are machined with a CO_2 laser, the coatings are applied externally. The surfaces of the mirrors can be measured in situ using white light interferometry with a Mirau objective, enabling iterative optimization of the geometry. In the course of this work, the control software for the fabrication facility, the method to reconstruct the mirror shape and the manufacturing procedure were developed. Furthermore, all necessary parts were produced and mostly set into place, enabling to start the prototype production soon. Due to their advantageous features for the construction of compact and robust quantum-enabled devices, their first application will be in the setup we are currently building in our group, which uses a tweezer array of neutral atoms inside a FFPC.

Zusammenfassung

Um unser Wissen zu vertiefen und zusätzliche Bereiche der Physik experimentell zu erschließen, scheint eine weitere Miniaturisierung der Technologien unumgänglich. Fabry-Perot-Interferometer FPIs, welche in der Regel aus zwei planparallelen Spiegeln bestehen und als Spektralfilter fungieren, stellen jene klassischen optischen Instrumente dar, welche die höchste spektrale Auflösung vor der Erfindung der Laserspektroskopie boten, und haben viele Experimente angeregt. Die Fortschritte bei der Bearbeitung der Endflächen von Glasfasern erlauben die Herstellung von faserbasierten Fabry-Perot-Resonatoren (FFPCs), kompakten Bauelementen mit kleinem Modenvolumen sowie einer offenen Geometrie und hoher Finesse. Sie können in vielen Bereichen eingesetzt werden, beispielsweise in der Sensorik, der nichtlinearen Optik und der Resonator-Quantenelektrodynamik CQED. In dieser Arbeit stellen wir einen hochautomatisierten Herstellungsprozess zur Fabrikation von FFPCs mit hoher Finesse vor. Während die Form der Spiegel mit einem CO_2-Laser erzeugt wird, trägt ein externes Unternehmen die Beschichtung auf. Die Oberfläche des Spiegels kann mittels Weißlichtinterferometrie unter Verwendung eines Mireau-Objektivs vermessen werden, wodurch eine iterative Optimierung der Geometrie ermöglicht wird. Im Rahmen dieser Arbeit wurden die Steuerungssoftware für die Fertigungsanlage, die Methode zur Rekonstruktion der Spiegelform und das Herstellungprozedere entwickelt. Darüber hinaus wurden alle notwendigen Teile beschafft und größtenteils montiert, sodass bald mit der Prototypenproduktion begonnen werden kann. Aufgrund ihrer vorteilhaften Eigenschaften für den Bau kompakter und robuster Quanten-basierter Geräte wird die erste Verwendung in jenem Quantensimulator stattfinden, welcher derzeit von unserer Gruppe aufgebaut wird und mithilfe von Tweezern neutrale Atome in einem FFPC anordnen wird.

Contents

1 Introduction

Prior to the development of laser spectroscopy, Fabry-Perot interferometers (FPIs) were the optical instruments with the highest spectral resolution and have stimulated many scientific insights. Consisting of two reflecting surfaces that constitute an optical cavity, it only transmits light that fulfills the resonance condition. Therefore, a FPI acts as a spectral filter. When working with macroscopic FPIs, the focus lies mostly on their reflecting and transmitting properties. However, the light field stored in between the mirrors is also of interest. By miniaturizing the geometry, smaller mode volumes with high optical access can be achieved and the slim footprint facilitates integration with optical fibers, thus posing promising candidates for quantum memories and repeaters. As technical progress advanced, end-facet treatment of optical fibers became feasible and enabled the fabrication of Fiber Fabry Perot cavities (FFPCs) with high finesses. One technique to achieve this was developed in 2010 by the group of Prof. Reichelt in Paris, where a CO_2 laser was used to evaporate the central part of an optical fiber and a high reflection coating was applied [1]. FFPCs can be used in many fields like sensing, nonlinear optics and cavity quantum electrodynamics (CQED). They additionally allow the exploration of more fundamental aspects of light-matter interaction. Furthermore, this strong coupling can be used to mediate interactions between different atoms inside the cavity.

The strong light-matter coupling that can be achieved with FFPCs is the main reason for its use in the new quantum simulator that is currently set up in the group of Prof. Leonard at the Atominstitute of the TU Wien. This quantum simulator works with ultracold neutral $^{87}\mathrm{Rb}$ atoms, which pose a promising platform for quantum information processing. Made feasible by laser cooling techniques, this experiment aims to take advantage of the long ranged photon mediated interactions, which are transmitted via the high-finesse cavity. A one dimensional tweezer array, whose trapping force is induced by the intensity gradient of a laser beam, is used to position the atoms inside the cavity. The overall goal is to engineer tunable non-local interactions between arbitrary subsets of atoms, allowing coherent manipulations of atomic states and giving rise to the possibility of entangling them.

The plan is to be able to load some tens or even a hundred or more atoms in the cavity with a spacing of about $1\,\mu\mathrm{m}$, requiring a distance of the mirrors on the order of $100\,\mu\mathrm{m}$ to $200\,\mu\mathrm{m}$. Extending the cavity leads to an enhanced size of the cavity mode at the mirrors. At some usually rather small distance below $100\,\mu\mathrm{m}$, the beam expands to regions of the mirror that deviate from the desired parabolic shape and do not support the cavity mode equally well as the central region does, leading to a significant drop of the finesse and hence the coupling strength. Since the currently commercially available fiber mirrors possess a rather small region in the order of $15\,\mu\mathrm{m}$ that supports the cavity mode reasonably well, the decision was made to produce fully customizable fibers in house. For that purpose a fiber fabrication setup has been established. The idea of the manufacturing process is as follows: Firstly, the vacuum compatible fibers are cleaved perpendicular to the core, creating a flat fiber tip. Secondly, the fibers are mounted to a 3-axis high-precision motorized stage and one tip at a time positioned close to the focus of a $9.3\,\mu m$ CO_2 laser. Thirdly, with one or more short pulses a part of the treated fiber is evaporated leaving a hole of the desired shape. Fourthly, the exact geometry can be obtained in situ using white light interferometry, allowing for iterative corrections of the profile. Fifthly, the fibers are sent to an external company where a high reflective coating is applied. Lastly, the fibers are tested and if approved, ready for being build into the quantum simulator.

This thesis consists of three main parts. In the beginning, the relevant theoretical background is summarized, focusing on the basic principles as well as characteristics of cavities and on the evaporation process of fused silicon when hit by a CO_2 laser beam. Afterwards, the setup of the fiber fabrication facility and the control software developed in the course of this thesis are presented in detail. Written in LabVIEW, the main control software connects the individual components and allows the automatization of many tasks. Thereafter, the surface reconstruction scheme using white light interferometry including the analysis method is introduced. The thesis is concluded by the review of the current status and the outline of the necessary subsequent steps for the production of the first prototypes.

2 Theoretical background

The theory relevant for comprehending this thesis is reviewed in this section. At first, FPIs in general and then specifically FFPCs are introduced, focusing on the most important parameters. Subsequently, the manipulation of optical fibers is discussed, including the description of their characteristics, the working principle of a CO_2 laser used for shaping the surface and the ablation process itself. Finally, the most relevant theory regarding the experiment in which the fibers will be primarily used, is denoted.

2.1 Optical resonators

An optical resonator or a cavity is a device, which consists of two or more reflecting elements, e.g. mirrors, that are arranged in a specific configuration to trap light waves inside the resonator. By design, the light repeatedly oscillates within the confined space, creating a strong light field. The fundamental principle of an optical resonator is based upon the concept of constructive interference. As the light waves travel back and forth between the mirrors, they interfere with one another. If the distance between the mirrors is an integer multiple of half the wavelength, the waves interfere constructively. Hence, the intensity of the light increases significantly within the resonator. This leads to a strong coupling to a medium when placed inside the cavity and is used in many applications like lasers, optical filters and optical amplifiers.

2.1.1 Fabry-Perot interferometer

Developed in 1897 by Charles Fabry and Alfred Perot, a FPI in standard configuration consists of two parallel partially reflecting surfaces facing one another. An alternative version that uses a single plate with parallel reflecting front- and backside is called Fabry-Perot etalon [2].

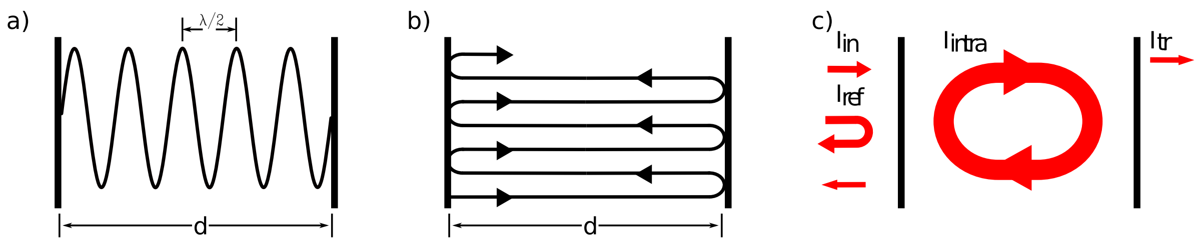

Figure 1: Sketch of the working principle of a FPI. a) Intensity of a resonator mode as a standing wave. b) Intracavity field as self sustaining traveling wave. c) Incoming, reflected, intracavity and transmitted intensities of a FPI. Sketch taken from [3].

Usually, the backside of a standard FPI is wedged and has an anti reflection coating applied to eliminate disturbing reflections. The distance between the mirrors can vary from micrometers to kilometers. When an optical wave reaches the interferometer, it is partly transmitted and partly reflected. The share entering the FPI, is repeatedly reflected back and forth as can be seen in the schematic diagram depicted by figure 1. In each cycle a small portion leaves the interferometer to both sides. In total four fields emerge: The incoming, the intracavity, the reflected and the transmitted field. Depending on the relative phases of the photons leaving the resonator at each cycle, constructive or destructive interference can occur. This behavior can be described with the Airy-formulae, which read for the transmitted intensity, when losses are negligible and perpendicular incidence of the light field on the resonator is assumed, as [4]

$$I_{tr} = \frac{I_{in}}{1 + \left(\frac{2\mathcal{F}}{\pi}\right)^2 \sin^2 \Delta\phi} \tag{1}$$

$$with \qquad \mathcal{F} = \frac{\pi\sqrt{R}}{1+R} \qquad and \qquad \Delta\phi = \frac{2\pi n d}{\lambda}\,. \tag{2}$$

Whereby n denotes the refractive index of the medium inside the FPI, $\Delta\phi$ stands for the phase accumulated when traveling along the distance d of the resonator once and $\mathcal{F}$ represents the finesse, which depends solely on the reflection coefficient R. For simplicity, symmetric mirrors with identical reflectivity are assumed here. From the Airy-formula for transmission can be seen, that an optical wave is transmitted maximally when the optical distance nd between the reflecting elements is an integer multiple of half the wavelength, yielding for a transmission peak the condition [5]

$$d = m\,\frac{\lambda}{2n} \quad for \quad m \in \mathbb{N}\,. \tag{3}$$

The distance $\delta\nu$ of two adjacent transmission maxima is called the free spectral range of the interferometer and given by

$$\delta\nu = \frac{c}{2nd}\,. \tag{4}$$

The sharpness of the transmission peaks, expressed in terms of the full width at half maximum (FWHM) $\Delta\nu$, is linked to the finesse, the most important quantity characterizing a FPI, via the relation

$$\Delta\nu = \frac{\delta\nu}{\mathcal{F}}\,. \tag{5}$$

Figure 2 shows the transmission spectrum of a FPI.

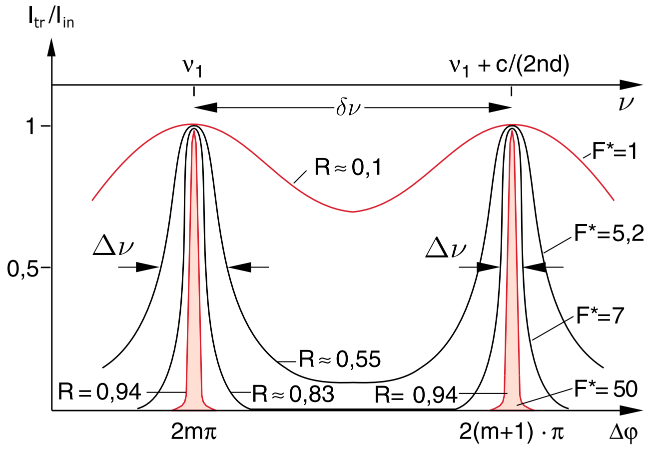

Figure 2: Sketch of the the transmission of a FPI. Transmission $T = I_{tr}/I_{in}$ at normal incidence of the light as a function of the phase difference $\Delta\phi$ for varying reflectivity coefficients R. Sketch adapted from [4].

2.1.2 Fiber Fabry-Perot cavities

When dealing with FPIs, the focus mostly lies on the transmitted respectively reflected intensity, giving rise to their use as spectral filters for instance. However, the strong light field stored between the reflecting elements is also of interest. Miniaturizing the geometry leads to a small mode volume with additionally a high optical access and enables integration with optical fibers [6]. Thanks to the technological advancement it is nowadays possible to machine mirrors onto the end-facets of optical fibers and utilize them to build FFPCs. Due to the strong light matter coupling featured, they pose a promising candidate for quantum memories and repeaters. Figure 3 shows the basic geometry of a FFPC. The eigenmodes of the resonator

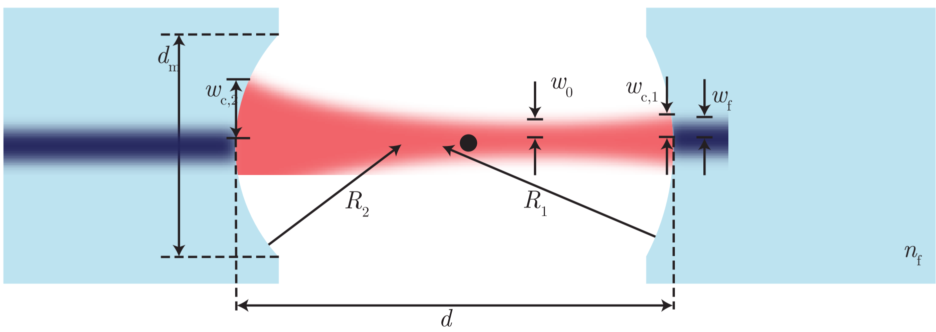

Figure 3: Sketch of the cavity mode. The mode waist w_0 is determined by the radii of curvature R_1 and R_2 and the cavity length d. For strong coupling, the mode sizes on the mirror, $w_{c,1}$ and $w_{c,2}$, have to be smaller than the mirror diameter d_m. Furthermore, the fiber mode size w_f and the refractive index of the fiber n_f influence the coupling. Sketch adapted from [7].

which emerge inside a cavity with spherical mirrors are Gaussian modes and are analogous to the eigenmodes of light propagation in free space. They are the solution of the paraxial Helmholtz equation [8]

$$\left(\frac{\partial^2}{\partial x^2} + \frac{\partial^2}{\partial y^2} - 2ik\frac{\partial}{\partial z}\right) E(x, y, z) = 0\,, \tag{6}$$

where $k = 2\pi/\lambda$ denotes the wave number and the beam propagates in z direction. Transforming the problem to cylindrical coordinates with $x^2 + y^2 = r^2$ and using the freedom to shift the origin to the center of the waist, yields as one solution

$$\psi(r, z) = E_0(z)\frac{w_0}{w(z)} e^{-i\left(\theta(z) + \frac{k}{2R(z)}r^2\right) - \frac{r^2}{w(z)^2}}\,, \tag{7}$$

with beam radius $w(z) = w_0\sqrt{1 + \frac{z^2}{z_R^2}}$, Rayleigh length $z_R = \frac{\pi w_0^2}{\lambda}$, Gouy phase $\theta(z) = \arctan\frac{z}{z_R}$ and curvature of the phase front $R(z) = \frac{z_R^2}{z} + z$. This equation describes the lowest order transverse electro-magnetic mode, TEM_{00}, known as the Gaussian or fundamental mode, which is the most widely used mode in cavities and schematically depicted in figure 4. It is the mode with the largest field strength at its waist.

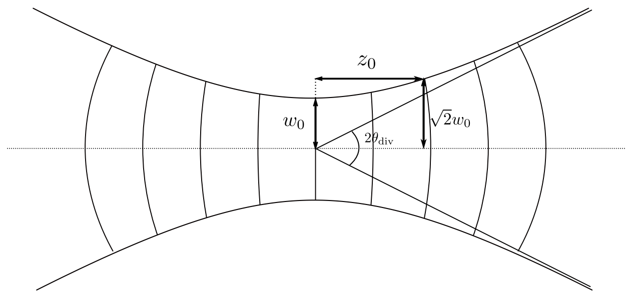

Figure 4: Sketch of the Gaussian fundamental mode and its wave fronts. The mode is defined by the three parameters waist w_0, divergence angle θ_{div} and Raleigh length z_0. Sketch adapted from [3].

Since the shape of the arising mode at the boundaries of the resonator resembles the profile of the mirrors, their radius of curvature determines in combination with the cavity length whether stable modes are supported. With the parameters $g_i = 1 - \frac{d}{R_i}$ one receives the stability condition

$$0 < g_1 g_2 < 1\,. \tag{8}$$

All stable configurations are shown by the stability diagram (figure 5). The geometry of a FFPC fixes the waist w_0 of the fundamental mode, which is given by [9]

$$w_0^2 = \frac{d\lambda}{\pi}\sqrt{\frac{g_1 g_2 (1 - g_1 g_2)}{(g_1 + g_2 - 2g_1 g_2)^2}}\,. \tag{9}$$

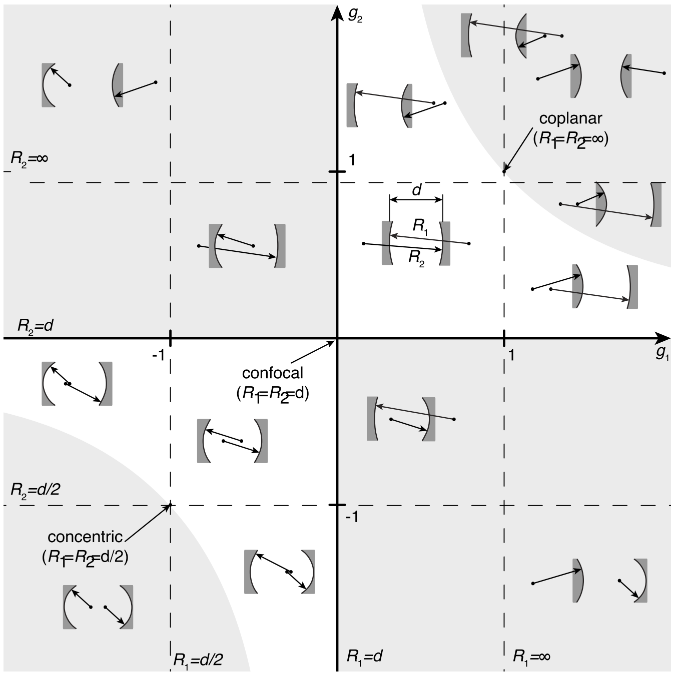

Figure 5: Stability diagram for cavities. Depending on the mirror parameters g_1 and g_2, stable (white) or unstable (gray) modes arise. The three special cases, concentric, confocal as well as coplanar lie on the stability edge. Sketch taken from [8].

Another important parameter, which affects the coupling strength of the cavity to the atoms, is the mode volume V_m of the FFPC. This quantity is a measure for the spatial confinement of the light field [10]

$$V_m = \frac{\pi}{4} w_0^2 d\,. \tag{10}$$

In cavity quantum electrodynamics (CQED), the single-photon coupling rate g expresses the interaction strength between an emitter and a coherent field. Considering a two level atom in a cavity, this quantity can be written as

$$g = \sqrt{\frac{3\lambda^3 c\gamma}{4\pi V_m}}\,, \tag{11}$$

with γ being the natural half width at half maximum (HWHM) line width of the atoms excited state and λ the cavity mode wavelength. This quantity depends on the resonator geometry via the mode volume V_m. In CQED, the single atom cooperativity C of a cavity is an important parameter, which describes the ratio of coherent over the incoherent processes and is given by

$$C = \frac{g^2}{2\kappa\gamma} = \frac{3\lambda^2}{\pi^3 w_0^2}\mathcal{F}\,, \tag{12}$$

with κ being the relaxation rate of the cavity. The second expression originates from a different approach but yields the same result. As demonstrated in [6], a simplified rate model computes the cooperativity as the ratio of the absorption cross section of the atom $\sigma = \frac{3\lambda^2}{2\pi}$ to the modal cross section of the photon $A = \pi w_0^2$ times the number of round trips a photon experiences in a cavity, which is determined by the finesse as $n_{round} = \frac{\mathcal{F}}{\pi}$. Reaching the strong coupling regime ($C >> 1$) requires a small mode waist w_0 and a high finesse. Both parameters can be tuned with the method presented in this thesis. The enhancement factor

$$\eta = \frac{2C}{1+2C}, \tag{13}$$

expresses the ratio of the emission rate of an initially excited atom into the cavity mode compared to the free space emission rate.

2.2 Shaping fibers

2.2.1 Optical fibers

Optical fibers are flexible dielectric waveguides, which transmit light with low losses over long distances. They consist of fused silica, SiO_2, which shows beneficial mechanical characteristics as it endures bending and bears significant pulling forces. By placing dopants like germanium dioxide, boron or titanium in the central region, an increase of the refractive index is introduced there. In this part, the so-called core, light traverses since at the interface with the surrounding cladding, total internal reflection occurs. The guiding properties can be influenced by the number of cores, their diameter and the refractive index profile [11]. While a single mode fiber can guide exactly one spatial mode, the TEM_{00} mode, multi mode fibers can transmit many spatial modes simultaneously, although in general over shorter distances. Another property by which multi mode fibers can be classified is the profile of their refractive index, giving rise to step- and graded-index fibers.

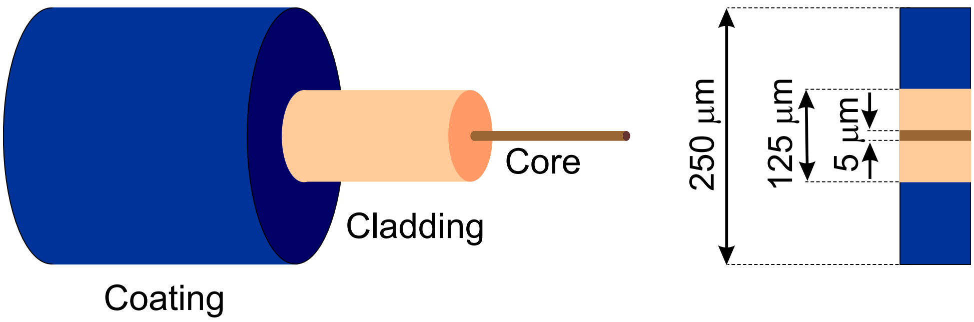

Figure 6: Sketch of a single mode optical fiber. It consists of a core, a cladding and a coating. Usual dimensions are given in the cross section. Sketch taken from [12].

Because of their advantageous properties optical fibers have become indispensable in telecommunication and optics technologies. On account of the low absorption they exhibit at the transition frequencies used in atomic experiments, they represent a useful instrument for quantum information apparati. In figure 7, which shows the absorption coefficient of fused silica in dependence of the wavelength, the high transmission of telecommunication wavelengths in the near infrared range ($780\,\mathrm{nm}$ - $3\,\mathrm{\mu m}$) can be seen on the one hand. On the other hand the peak at roughly $9.3\,\mathrm{\mu m}$, which originates from an asymmetrical Si-O-Si vibrational resonance [13], stands out. This property of fused silica can be used to precisely evaporate material at the desired position.

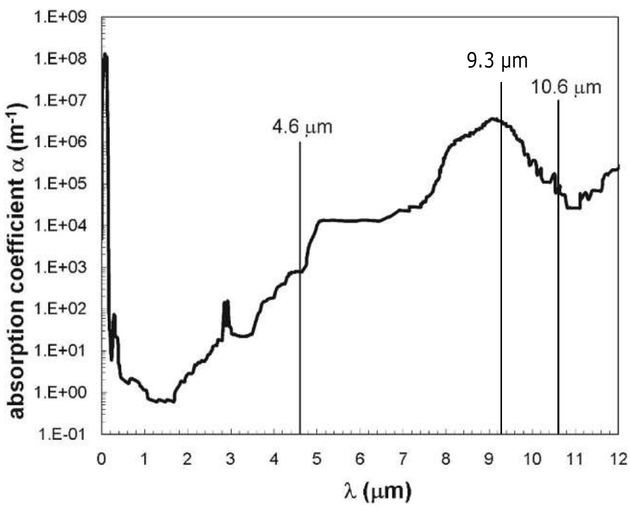

Figure 7: Absorption spectrum of fused silica. The peak at $9.3\,\mathrm{\mu m}$ originates from an asymmetrical Si-O-Si vibrational resonance. Sketch adapted from [14].

2.2.2 Carbon-dioxide Laser

In a carbon-dioxide laser, the active medium is a gas mixture containing CO_2, N_2 and He, with varying percentages depending on the application. Due to its efficiency, which ranges up to 20%, as well as its reasonable pricing, the carbon-dioxide laser is regularly used in industry. Vibrational modes of N_2 molecules are excited via DC- or RF-gas discharges. Since nitrogen is a homonucleus molecule and therefore possesses no permanent dipole moment, it cannot lose energy via the emission of photons, as the corresponding transitions are forbidden. Hence, these states are meta stable and pose a high probability to collide with CO_2 molecules. As these two species possess nearly resonant energy levels, in this process N_2 can be de-excited and CO_2 excited in return. From this level, the asymmetric stretch vibrational mode, carbon-dioxide then radiatively emits a photon with a wavelength in the range from approximately $9\,\mathrm{\mu m}$ to $11\,\mathrm{\mu m}$ by transiting to the bending respectively symmetric-stretch vibrational mode. The most prominent emission lines lay at $10.6\,\mu\mathrm{m}$, $10.2\,\mu\mathrm{m}$, $9.6\,\mu\mathrm{m}$ and $9.3\,\mu\mathrm{m}$. Afterwards, the CO_2 molecules de-excite via collisions with cold helium atoms, sustaining the necessary population inversion. To maintain this process, the heated helium atoms need to be cooled. While, depending on the laser power, air or water cooling are applicable, the latter poses the advantage of being quieter, producing less vibrations as well as maintaining a more stable temperature and hence more constant power output.

2.2.3 Ablation process

When a laser beam hits a material, it is partly absorbed. The amount of energy transferred to the material and the absorption depth depend on the absorption characteristic of the material and the wavelength of the laser. If the laser can be absorbed reasonably well, particles in the uppermost layers receive enough energy to be evaporated, leading to the ablation of the surface. As described above, the absorption peak of fused silica around $9.3\,\mu\mathrm{m}$ can be used to machine optical fibers by ablation. Hence, CO_2 lasers whose wavelengths are in this range, are an ideal tool to accomplish this task. They allow to create depressions with an approximately Gaussian profile and a low surface roughness due to the balance between evaporation and melting [15]. For a crater to be eligible as a cavity mirror, it has to feature a low ellipticity and a very smooth surface. Furthermore, its shape has to support the desired cavity mode. Commonly, as in our case, the fundamental mode described in section 2.1.2 is used. Since its phase front is parabolic, the mirror has to fit this profile. By applying an axially symmetric Gaussian beam pulse, this condition can be met in the center. Modifying the laser power, the pulse duration and the beam waist enables to carve different forms into the uppermost layers, whereby the most important parameters of the created profile are the radius of curvature in the center and the size of the parabolic region. This can be showed as follows: It has been theoretically shown that conditioning fused silica with ideal Gaussian laser pulses from a stable source featuring an ideal intensity distribution $I(r) = I_0\, e^{\frac{-2r^2}{w_0^2}}$, produces a pit whose depth profile is given by

$$z(r) = z_0 e^{-\frac{U}{k_B T(0,\tau)}\frac{r^2}{2w_0^2}} \,. \tag{14}$$

Here $U = 3.6\,\mathrm{eV}$ is the latent heat of evaporation per atom, k_B the Boltzmann constant, z_0 the depth of the crater in the center and w_0 the waist of the laser beam. $T(0,\tau)$ expresses the temperature in the center after being hit by a pulse of duration τ and is given by

$$T(0,\tau) = \frac{A(\lambda)P}{\sqrt{2\pi^3}\, w_0 \kappa} \arctan \frac{2D}{w_0^2}\tau \,, \tag{15}$$

with the thermal conductivity κ, the wavelength dependent absorption coefficient A, the laser Power P and the thermal diffusion coefficient D. This temperature distribution is determined analytically from the two dimensional heat conduction equation. However, this model is based upon several assumptions and idealizations like an infinite surface and ideal absorption in the uppermost layer. Therefore, it is remarkable that the theory describes the carved shapes on a fused silica plate well [16]. Nevertheless, on a fiber with limited dimensions, the heat does not propagate as analytically assumed, yielding deviations from the ideal profile [15] . Further neglected effects are the energy loss due to black-body radiation, a non linear thermal conductivity and a not perfectly rectangular laser pulse. Moreover, it is assumed that we are in the regime where lateral heat transport is the dominant cooling mechanism and the energy loss via the kinetic energy of evaporated particles is negligible. Hence, the velocity of the evaporation front defines the profile after a given illumination time[17]. From the number of assumptions made, it can be guessed that it is very challenging to accurately predict the resulting profile, making experimental tests inevitably. It has been shown, that by tuning the three parameters laser power, pulse length and beam waist, depths $z = 10\,\mathrm{nm}$ - $4\,\mathrm{\mu m}$ and radii of curvature $ROC = 5\,\mathrm{\mu m}$ - $2\,\mathrm{mm}$ can be carved [18] In addition, these parameters have to be selected with care, such that the material removal occurs because of thermal evaporation. A thin layer of molten silica, however, is actually desired since it smoothens the surface on an atomic scale due to surface tension, but has to stay slim enough to not produce convex structures.

2.3 Quantum information processing with FFPCs

In this section, the basic ideas of the experiment for which the fibers will be primarily used, is introduced. Here, only the most prominent features and the fundamental principles are portrayed.

2.3.1 Cavity Experiment

Depicted by figure 8, the quantum simulator currently being build up in the group of Prof. Leonard at the Atominstitute of the TU Wien in Vienna is designed as a versatile and universal platform for CQED experiments with individually addressed atoms. It uses a tweezer array to position neutral $^{87}\mathrm{Rb}$ atoms inside a FFPC, to whose field all atoms are strongly coupled. Each atoms' state can be prepared, evolved, and afterwards read out with high fidelity. By microscopically addressing each single atom, the coupling strength to the cavity mode can be individually adjusted. Moreover, this feature can used to mediated tuneable interactions between arbitrary subsets of atoms, giving rise to a large number of possible applications. This setup poses several demands to the FFPC: On the one hand, the cavity has to be as large as possible to hold as many atoms as feasible and to provide optical access to all needed laser beams. On the other hand, the coupling to the FFPC has to be as strong as possible (high cooperativity C) to achieve high fidelities for all operations. These two requirements are in general competing since a larger cavity leads to an enhanced size of the cavity mode at the mirrors. Therefore, the region of the mirrors that supports the cavity mode well has to be as large as possible. As can be seen from equations (9), (10), (11), (12) and (13), the relevant parameters regarding the coupling strength are the radius of curvature and the finesse. While the finesse has to be as high as possible, the radius of curvature has to be chosen in way that the mode volume V_m at the center of the cavity is small and the stability criterion (8) is well met. The currently used cavity is in the quasi co-planar region, which leads to a relatively large area in the center with only a small variation of the beam size, yielding roughly constant coupling strengths to the atoms at different locations. In general it is conceivable to also use con-focal or concentric configurations. As the desired length of the FFPC is $100\,\mu\mathrm{m}$ to $200\,\mu\mathrm{m}$, the radius of curvature needs to be of the same magnitude.

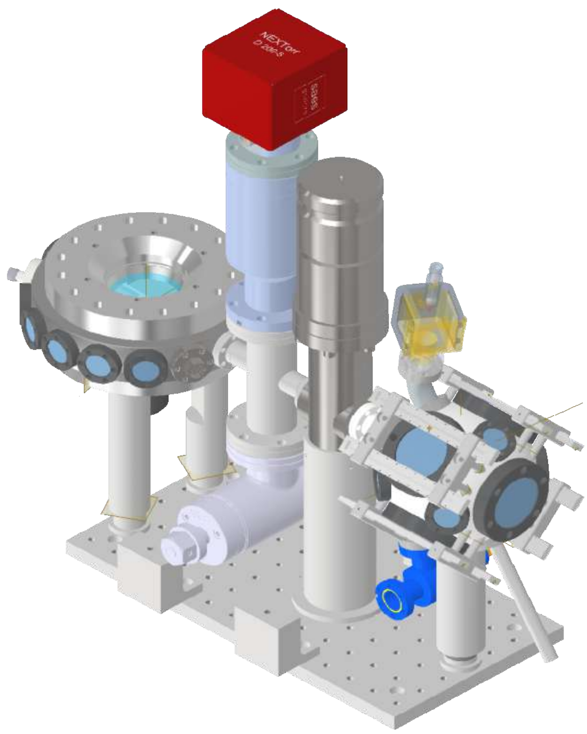

Figure 8: Sketch of the Leolab cavity experiment. It uses a tweezer array to position neutral ^{87}Rb atoms inside a FFPC. Sketch taken from [19].

2.3.2 Jaynes-Cummings hamiltonian

The principal reason for the use of a FFPC in the quantum simulator is that it provides a strong confined light field to which the atoms couple, yielding a hybrid photon-atom system. The simplest way to theoretically model this process results in the Jaynes-Cummings hamiltonian, which describes the coupling of a single light frequency ω_c to a two level system. In the rotating wave approximation it is given by the expression

$$\hat{\mathcal{H}}_{JC} = \hbar\omega_a \hat{\sigma}_+ \hat{\sigma}_- + \hbar\omega_c \hat{a}^\dagger \hat{a} + \hbar g(\hat{\sigma}_+ \hat{a} + \hat{\sigma}_- \hat{a}^\dagger)\,, \tag{16}$$

with $\hbar\omega_a$ being the energy difference of the two atomic levels, the atomic raising ($\hat{\sigma}_+$) and lowering ($\hat{\sigma}_-$) as well as the photonic annihilation ($\hat{a}$) and creator ($\hat{a}^\dagger$) operators and the coupling strength $g = \frac{\mathcal{D}\mathcal{E}_{max}}{\hbar}$, which depends on the dipole moment $\mathcal{D}$ and the strength of the lights' electric field $\mathcal{E}_{max}$ [20]. The interaction term, which is the latter part, has an ostensive physical interpretation: While its first expression describes the absorption of a photon and the subsequent excitation of the atom, the second term describes the reverse process, i.e. emission of a photon induced by de-excitation of the atom. Hence, the total number of excitations is a conserved quantity, which hints to the block diagonal form of the hamiltonian. This property allows to find an analytical solution. The corresponding eigenenergies of the so-called dressed eigenstates form the Jaynes-Cummings energy ladder, which is depicted in figure 9. As can be seen, the splitting of the energy levels depends on the square root of the number of total excitations, giving rise to a non-linear spectrum. This non-linearity is the source of the photon blockade mechanism: if a photon is present in the system, the interaction with further photons is frustrated, no matter how large the flux density of the incident light is. Furthermore, the non-linearity is the fundamental process for a variety of applications, like quantum memories, quantum repeaters, single-photon sources, and can be used to entangle atoms at different tweezer locations in the cavity, which is one of the most interesting properties for the experiment at hand.

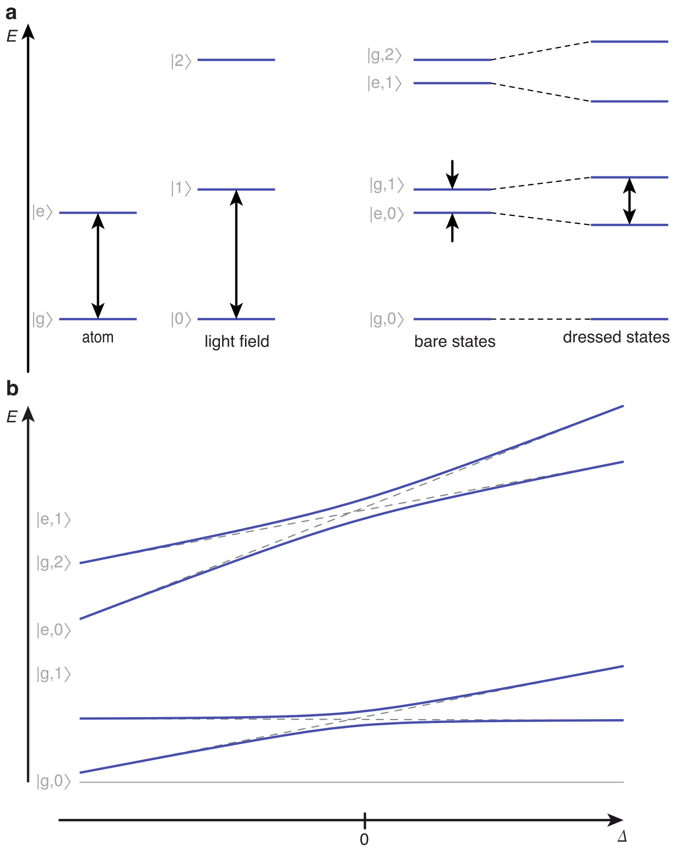

Figure 9: Jaynes-Cummings energy ladder. a) The atom is modeled as a two-level system with ground state $|g\rangle$ and excited state $|e\rangle$. The light field exhibits a energy ladder of equally spaced levels, ascending with the photon number $|n\rangle$. The photon energy and the atomic transition energy are similar. The atom-light coupling causes a repulsion between adjacent levels with dressed states as eigenstates of the combined system. b) Energy of the dressed states as a function of the detuning of the photon energy and the atomic transition energy. We find an avoided crossing when two energies approach one another. Figure taken from [8].

3 Experimental Setup

In this section, the experimental setup used for fabricating and analyzing the profiles machined onto the end facets of optical fibers is presented. The main steps in this process are, firstly, the localization of the center of the fiber and the CO_2 laser beam, secondly, the ablation of the fiber tip with a laser pulse, thirdly, the interferometric measurement of the created depression and, lastly, the application of a high reflective coating, a step which is outsourced to a specialized company. At the beginning of this section, the hardware components of the setup are introduced. This includes the characterization of a CO_2 laser used for ablation and its controller, the description of infrared optics and the specification of a 3-axis motorized stage, which maneuvers the fibers. Moreover, with a power meter, a Mirau objective, a camera as well as further parts of the interferometry section, the devices used for measurement are delineated. Subsequently, the developed software programs that control, on the one hand, the laser directly and, on the other hand, all components from a single graphical user interface, are portrayed.

3.1 Hardware

Figure 10 schematically depicts the whole experimental setup. While in the upper section the fabrication part can be seen, the lower area shows the interferometry setup. A 3-axis motorized stage can position the fibers with high precision and transfers them between the fabrication and the interferometry zone. A power meter is not indicated here, it is located behind the stages in the direction of the CO_2 laser beam.

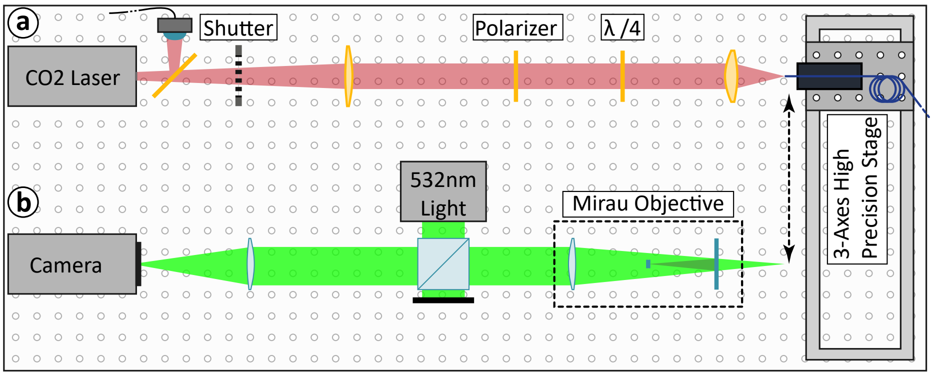

Figure 10: Sketch of the setup. The upper section depicts the fabrication part, while in the lower area the interferometry part can be seen.

3.1.1 Fabrication part

This section of the experimental setup consists of all components that are necessary to shape fibers. The first device is a Coherent Diamond C-55 Liquid-Cooled OEM Laser, a CO_2 laser emitting light with a wavelength of $9.3\,\mu\mathrm{m}$. According to the data sheet, the diameter $(1/e^2)$ of the beam is $1.8\,\mathrm{mm}$ and the full angle divergence $7.5\,\mathrm{mrad}$. It is water cooled with a minimal flow rate of $3.8\,\mathrm{L}$ per minute, a maximum pressure of $3.2\,\mathrm{bar}$ and a coolant temperature between $15\,^{\circ}\mathrm{C}$ and $30\,^{\circ}\mathrm{C}$. The cooling liquid is filtered to avoid the accumulation of debris in the cooling system. An in-house build power source supplies a direct current to the laser with a voltage of $48\,\mathrm{V}$ and an amperage of $20\,\mathrm{A}$. The laser can either emit the full laser power of approximately $50\,\mathrm{W}$ or nothing. Continuous and single pulse mode are supported. In the continuous pulse mode, the output of the CO_2 laser is switched rapidly. The ratio of the time the beam is emitted to the full duration of a period, the so-called duty cycle, determines the average laser power. According to the manual, switching frequencies up to $25\,\mathrm{kHz}$, i.e. duty cycles down to $40\,\mu\mathrm{s}$, and single pulse durations as low as $1\,\mu\mathrm{s}$ are supported. The output of the CO_2 laser is triggered via a RJ-45 port. A Teensy 4.1 micro controller is utilized for this task. Via a customized pinboard containing signal LEDs, it is connected to the laser, the water flow sensor and a USB port of a computer. It sends the status of the laser as well as the flow rate to the computer and, depending on the messages received from the computer, sends the operational commands to the laser. Here, two particular signals have to be mentioned. The first is the control-enable-signal. If a voltage is applied to the corresponding RJ-45 pin and the internal laser controller senses no condition that opposes operation, the laser is in *ready to shoot* mode. Only when the laser is in this mode, the second notable signal, the on-signal, leads to the emission of laser light.

Figure 11 shows the output of the laser and the following components. The subsequent ZnSe window serves two purposes. On the one hand, it reflects a small share of the laser light to the beam dump. This component can be replaced by a power meter to measure the intensity of the beam during operation. This will be especially useful when in the future an acousto-optical modulator (AOM) is inserted between the laser and the window, since it enables power stabilization via a feedback loop and additionally the generation of arbitrary intensity profiles. On the other hand, the window allows to overlap a green pilot laser beam which is guided by a single mode fiber with a yellow jacket to the adjacent collimator with the CO_2 laser beam. The green light is used for pre-alignment, as it is easily visible and poses almost no health risk in contrast to the $9.3\,\mu\mathrm{m}$ light at low power. After traversing the window, the polarization of the laser light has to be changed from linear to circular as the next step. This is necessary since a linearly polarized beam would result in an elliptic shape on the fiber tip. Due to the fact that commonly used optical elements like lenses and quarter-wave plates (QWPs) are made out of fused silica and therefore, as described in section 2.2.1, absorb the $9.3\,\mu\mathrm{m}$ light in the uppermost layers which then evaporate, they cannot be used. Hence, special infrared compatible optics are used in this setup, mainly components which are based

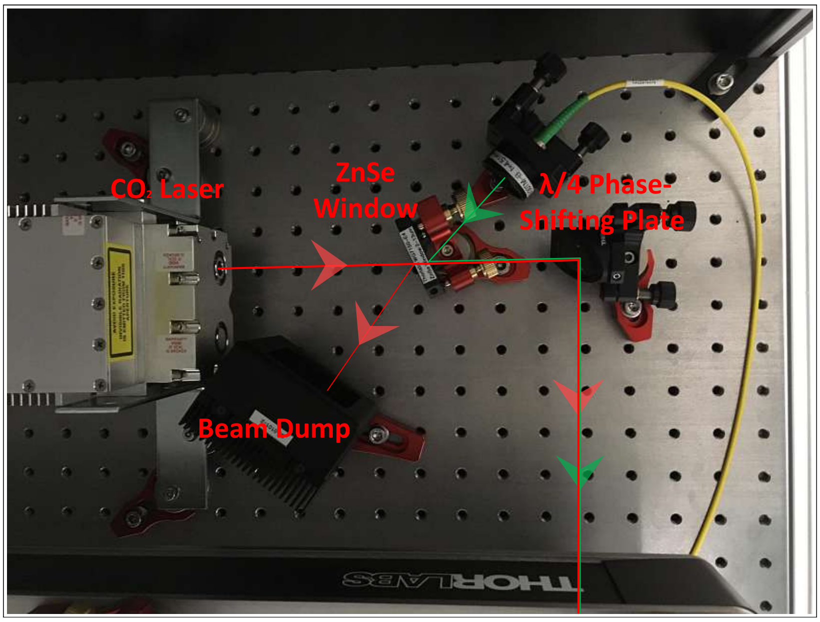

Figure 11: Picture of the laser output. The 9.3 µm light from the CO_2 laser traverses the ZnSe window and its polarization is changed from linear to circular at the $\lambda/4$ phase-shifting plate. The green light is used for pre-alignment. At the position of the beam dump, a power meter can be placed for measuring the intensity during operation.

on ZnSe or coated with gold. For changing the polarization, a phase-shifting ($\lambda/4$) mirror is utilized. Due to the geometric requirements for this modification, specifically concerning the planes of incidence and reflection, the phase-shifting plate has to be rotated by 45° around the pitch and yaw axis with respect to the beam axis (which represents the roll axis). As the reflected beam is going upwards and thus does not travel in the plane parallel to the table any more, the subsequent optics are located on a higher level. After the modification of the polarization, an accordingly tilted mirror reflects the beam in parallel to the upper breadboard. Subsequently, the two gold coated mirrors are used to align the beam onto the final converging lens.

This configuration, as shown in figure 12, provides full control over the direction as well as the position of the outgoing beam. Since the following element is the ZnSe focusing lens with a focal length of 100 mm, this functionality is essential to align the laser with respect to the axis of the lens. A perfect overlap is needed here to avoid the introduction of aberrations and to maintain a Gaussian beam profile behind the lens, especially at the focal point. To this region the fibers, other targets and razor blades used for a so-called knife edge test (see section 4.1) to identify the beam shape, are moved by a 3-axis motorized translation stage. This structure consists of 3 individual stages from Newport, which can move in the x- (XML210-S), y- (XMS50-S) and z- (MLT25-Z) direction respectively. They have a minimal stepsize of 1 nm and a bi-directional repeatability of 20 nm, meaning that if the stage is moved to a completely

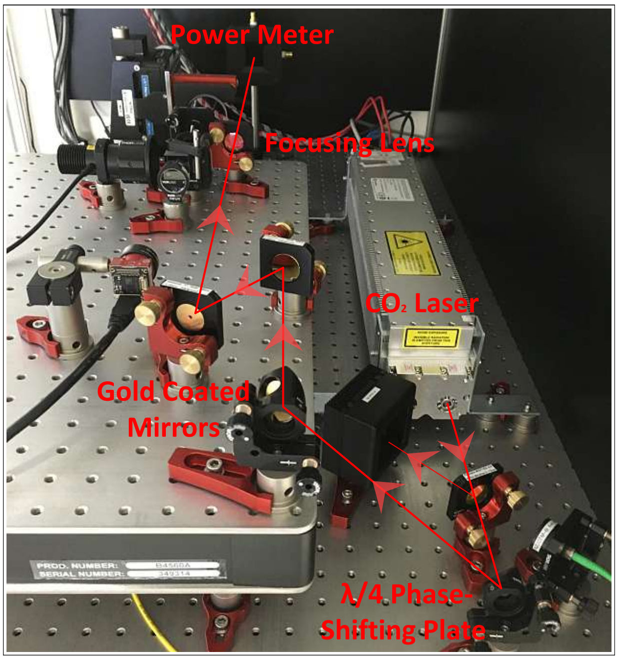

Figure 12: Picture of the full setup. The laser light that travels from the $\lambda/4$ phase-shifting plate upwards is reflected in parallel to the breadboard. Via two gold coated mirrors it is sent to the focusing lens, traverses the manufacturing zone and hits the power meter.

different location and then back, the position is accurate down to this number. All stages are steered via a common controller (Newport XPS-D6), which is accessible via an Ethernet cable. Behind the stages, the beam hits a power meter PowerMax 150 HD from Coherent, that is accessed via a LabMax-Pro SSIM controller. It measures the incident laser power thermally and its active region measures $30\,\mathrm{mm}$ times $30\,\mathrm{mm}$. It has a rising and falling time below $10\,\mathrm{\mu s}$ and can handle continuous powers up to $150\,\mathrm{W}$.

3.1.2 Interferometry part

The interferometry part, depicted by figure 13, consists of three main components. The first is the broad band LED source with a center wavelength of $554\,\mathrm{nm}$ and a spectral width of approximately $100\,\mathrm{nm}$. Via a non polarizing beam splitter (NPBS) the light is sent to the second principal part, the Mirau objective (Nikon CF IC EPI PLAN DI 20X), which has a numerical aperture of $NA = 0.4$, a working distance of $4.7\,\mathrm{mm}$ and a focal length of $9.97\,\mathrm{mm}$. This device exhibits, apart from the usual focusing ability of an objective, a semi-transparent window at the front, that reflects a share of the light to an internal reference mirror. This design allows to build a compact interferometric setup. Its working principle is presented in section 4.2, together with the whole surface analysis procedure.

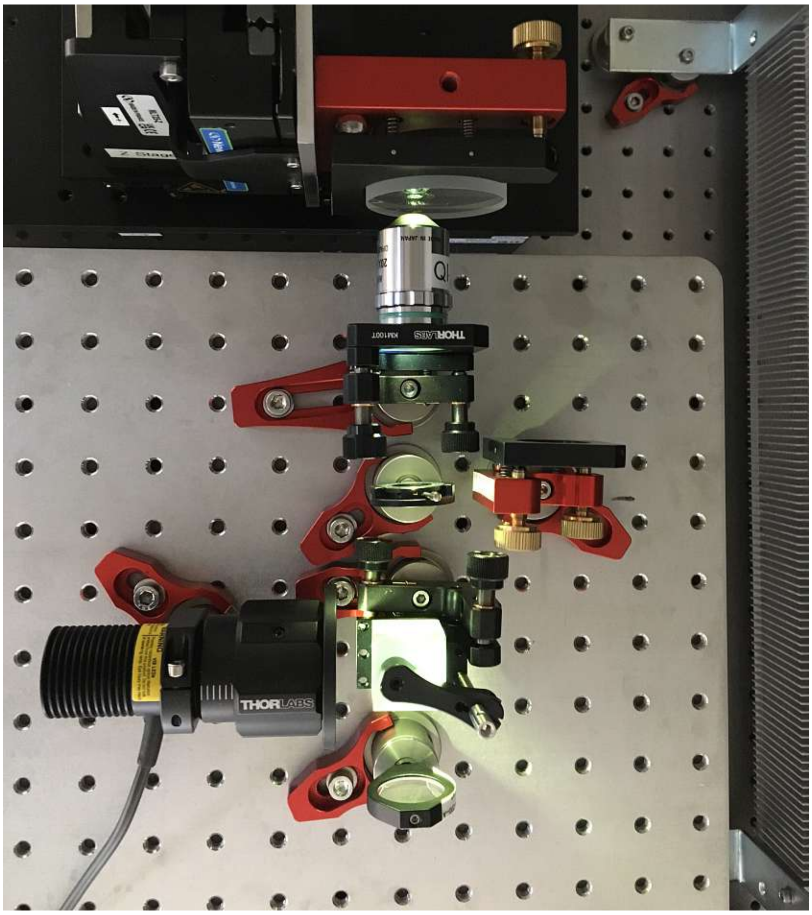

Figure 13: Picture of the interferometry part. The light from the LED is reflected by the NPBS and reaches the Mirau objective. There it is focused and via the semitransparent window guided to the two paths. While the first leads to the internal reference mirror, the second passes to the sample, which is glass plate here. The reflection from the sample interferes with the light from the reference path, is expanded by traversing the Mirau objective in the reverse direction and transits the NPBS. Afterwards, a concave lens with a focal length of 200 mm projects the resulting interferogram onto the camera (not shown).

The sample, usually a fiber tip, is moved to the focal point of the Mirau objective by the 3-axis motorized stage, allowing this process to be automated and to swiftly move the fiber after fabrication to the interferometry station. After the two beams from the different paths have interfered, they leave the objective at the backside, traverse the NPBS and reach a concave lens with a focal length of $200\,\mathrm{mm}$, which projects the interferogram on an Alvium 1800 U-319 camera. The sensor of this CMOS camera has 2064 x 1544 pixels, each one being quadratic with a side length of $3.45\,\mathrm{\mu m}$, and a 12 bit resolution. Its pictures are then directly fed to the computer, where they are used to reconstruct the surface of the fiber.

3.2 Software

In this section, the control scripts which were developed and extended in the course of this thesis are described. At first the program which is run on the Tennsy 4.1 to control the CO_2 laser is introduced. Thereafter, the main experiment control software, which integrates the individual components, is described. The codes are available to the interested reader upon reasonable request.

3.2.1 Laser control software

The program run on the Teensy 4.1 uses the same logic like the ones Arduinos are run with. The main idea, as indicated by figure 14, is that, after the initialization is done, a loop, which processes the voltages at the input pins and sends signals to the output pins, cycles repeatedly. This software is implemented as a `C++` file in the integrated development environment *PlatformIO*. At first, all variables are defined and the methods to update the status of the laser and the method to count the pulses from the water sensor are specified. For the status update, the input from the laser and the switches on the pinboard as well as the current water flow are considered. This method also refreshes the control LEDs. The method to count pulses is used for the measurement of the water flow, which is needed to check whether the laser is adequately cooled. Since the program operates in general serially and the signal of the water flow sensor has to be measured continuously, a special construction is needed to accomplish this task. The method to count the pulses from the water flow sensor is attached to the corresponding pin of the Teensy 4.1 as an interrupt function. This means, that this function is called every time the signal changes in the specified way, independently of the main loop. After the definitions, the initialization routine is called, which inter alia specifies the input and output pins as well as sets the pulse-width modulation (PWM) resolution and frequency.

Hereinafter, the main loop starts to run repeatedly. For performance reasons, the water flow value and the status of the laser are updated only every second and not in each cycle. If due, the number of pulses since the last update is used to compute the current flow rate and the status variable of the laser is refreshed. Afterwards, the program checks whether a command is pending at the serial port and processes it as the case may be. Since the loop is intended to run continuously and the whole logic is based on a rapid consecutive execution, *wait* commands have to be circumvented whenever possible. Therefore, the variable *mode* keeps track of the laser mode. Its possible values are 0 ("laser off"), 1 ("continuous pulses") and 2 ("single shot") and are changed by the received commands. To reassure that the message was obtained correctly, the received byte is sent back to the serial port with the prefix *rec*. There are five possible messages that can be obtained. The basic commands 0, 1 and 2 set the variable *mode* to 0, 1 respectively 2. The message 3 has two bytes appended that determine the duration of

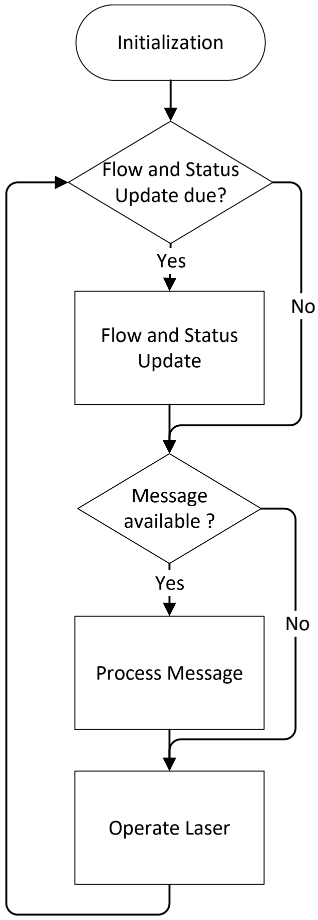

Figure 14: Flow diagram of the laser control software.

a single shot. When the command 4 together with its appended data byte are received, the laser power for continuous pulse operation is adjusted. If an unknown message is present at the serial port, it is discarded. Furthermore, in the last three cases the variable *mode* is set to 0 for safety reasons. In each case a message expressing the performed action with the prefix *msg* and a timestamp is written to the serial port.

The last section of the loop is executed every cycle and depends on the current value of the variable *mode*. If it is 0, no voltage is applied to the pin that controls the laser output. When it has the value 1 and the laser is ready to shoot, a PWM signal with the chosen duty cycle percentage is forwarded to the laser. In case the variable *mode* was set to 2 and the laser is ready to shoot, a single pulse with the selected duration is sent to the laser. Afterwards, the variable *mode* is set to 0 and the loop starts anew.

3.2.2 Experiment control software

The main experiment control software is written in LabVIEW. This choice was made, since the program poses a versatile platform explicitly designed to control experiments. It provides the possibility to integrate a wide range of devices and to process multiple input signals simultaneously. Moreover, it allows to add as well as remove components during runtime and is based on C++, therefore it is inherently fast. The principal purpose of this program is to operate all devices of the experimental setup from a single control panel and to automate as many functions as possible. Since all components run simultaneously, the program has to reproduce this behavior in its architecture and moreover has to enable the communication between them. To meet these requirements, the actor framework is used. It is an implementation of the actor model whose maxim is that everything is an actor. Starting from the unique root actor, the actors form a treelike hierarchy, with each actor bearing the potential to launch further so-called nested actors. The communication between the actors is handled via messages, whereby it is suggested that an actor only sends message to itself, its calling actor (except the root actor, who has no calling actor) and its nested actors. A message can either lead to the execution of a subroutine, change the state of an actor, cause a nested actor to be launched or trigger another message.

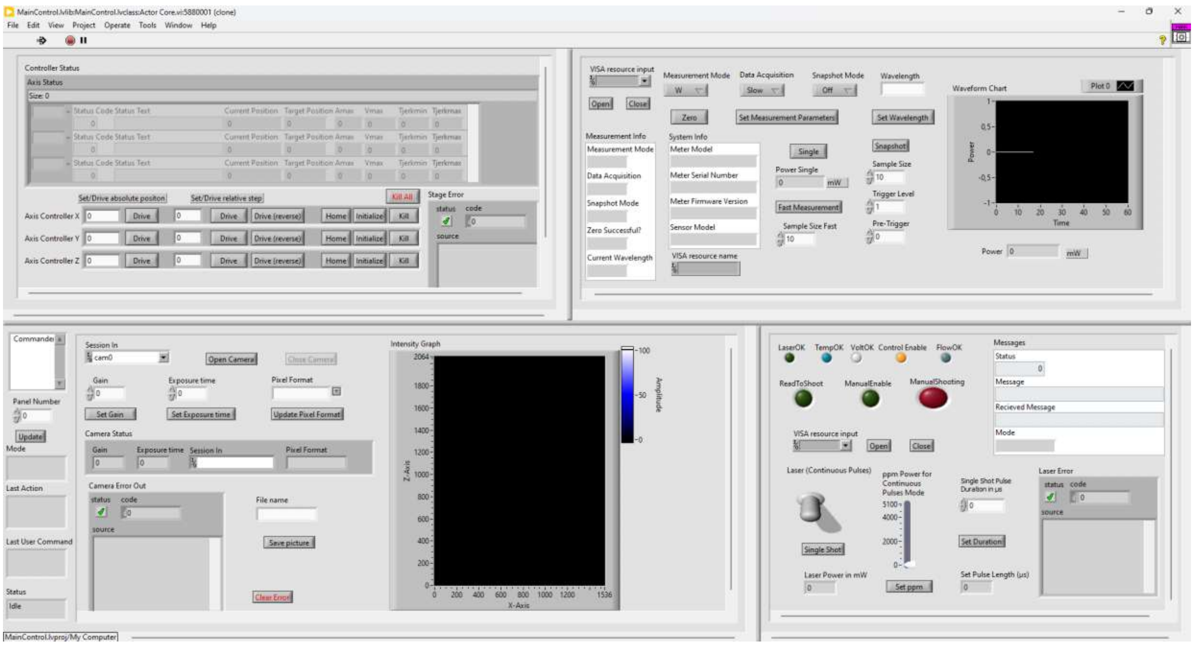

Figure 15: Picture of the front panel of the *Main Controller* actor. In the four sub-panels, the front panels of nested actors are shown. In the left lower corner, the controls for changing the actors visible in the sub-panels are located and status information is depicted.

The global architecture of the experiment control software is rather simple, since it consists of six actors and only two hierarchy levels, with the *Main Control* actor as root actor on top and the other five actors as its nested actors. Therefore, all messages are either sent or received by the root actor. The front panels of the nested actors are all integrated into sub-panels of the front panel of the *Main Control* actor as shown in figure 15. This view appears when the program is stared via the *Launcher.vi*. Since there are only four sub-panels but five nested actors, the name of the currently not visible actor is depicted in the listbox located in the left lower corner and will be shown at the selected location (*Panel Number*) upon pressing the button labeled *Update*. Further actors can be integrated easily into this mechanism, providing full customizability. Thereby the options $0-3$ refer to the left upper, right upper, left lower and right lower sub-panel in this order. Furthermore, in the left lower corner useful data is depicted. This data incorporates the information regarding the current mode of the *Main Control* actor, its last action, its status and the last user command received. The five nested actors are named *Stage Controller*, *Powermeter Control*, *Camera Control*, *Laser Controller* and *Commander*. While the first four control the corresponding devices in the experiment, either directly or via intermediate controllers, the purpose of the *Commander* actor is to trigger elaborated routines that require the interaction of more than one component, like the knife edge test described in section 4.1.

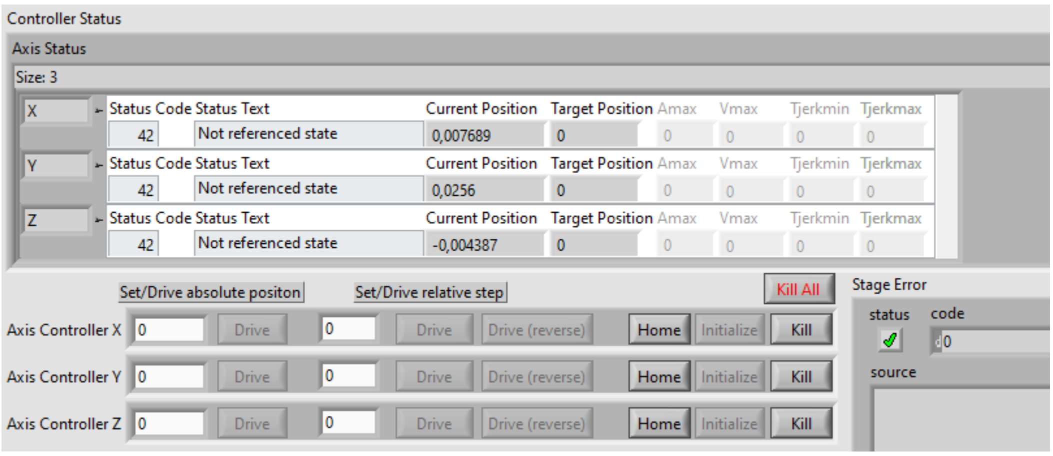

Figure 16: Picture of the front panel of the *Stage Controller* actor. While in the upper section the current status is shown, the controls in the lower section serve to operate the stages.

The *Stage Controller* actor, whose front panel is depicted by figure 16, communicates with the Newport controller of the stages via an Ethernet connection. Upon launching, the link between the computer and the controller is established. Afterwards, all three stages have to be initialized and homed individually, before they can be moved to an absolute position or by a relative distance. Meanwhile, in the upper part of the control panel, the current status of all axis including the current and target position as well as the status code and text is displayed and updated every $250\,\mathrm{ms}$. Furthermore, additional values like the upper limits for velocity and acceleration are shown upon request. When scrolling down, one reaches the controls to adjust them. The main task of this actor is to move the stages and report their status.

Via a serial connection, the *Powermeter Control* is linked to the control unit of the power meter. Its front panel is depicted by figure 17. After the actor has been launched, the correct USB port has to be chosen to open the VISA connection. When this procedure was successful, the information regarding the measurement and system are displayed in the lower left section. Afterwards one has to zero the power meter, whereby the laser beam has to be blocked. With the controls in the upper region of the panel, the measurement parameters, like the data acquisition speed, the snapshot and measurement mode as well as the wavelength can be adjusted. With the controls in the middle either a single, fast or snapshot measurement can be performed. To the right, a waveform chart shows the trend of the recorded power for the last minute and an indicator shows the currently measured power. The update interval is one second. The principal task of this actor is to provide the current power value.

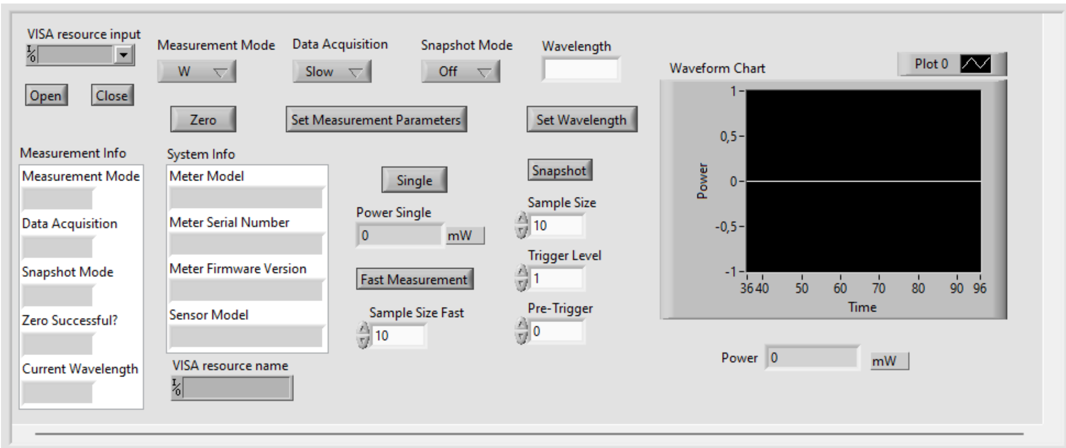

Figure 17: Picture of the front panel of the *Powermeter Control* actor. The controls in the upper section serve to establish the connection to the power meter and to adjust measurement values. In the lower left area, status information is given. With the controls in the middle a single, a fast and a snapshot measurement can be performed. To the right the current power value is depicted as well as the trend over the last minute.

The actor *Camera Control* uses the build-in IMAQ functions and driver in LabVIEW to control the camera. By pressing the button *Open Camera*, the connection to the selected camera is established via an USB link. If successful, its status is displayed in the corresponding line. Via the overlying controls and buttons, the gain, acquisition time as well as pixel format can be changed. The button *Make picture* saves a single frame to a hard-coded directory. To the right, an intensity graph shows the current acquired image and is updated every second. Its front panel is depicted by figure 18.

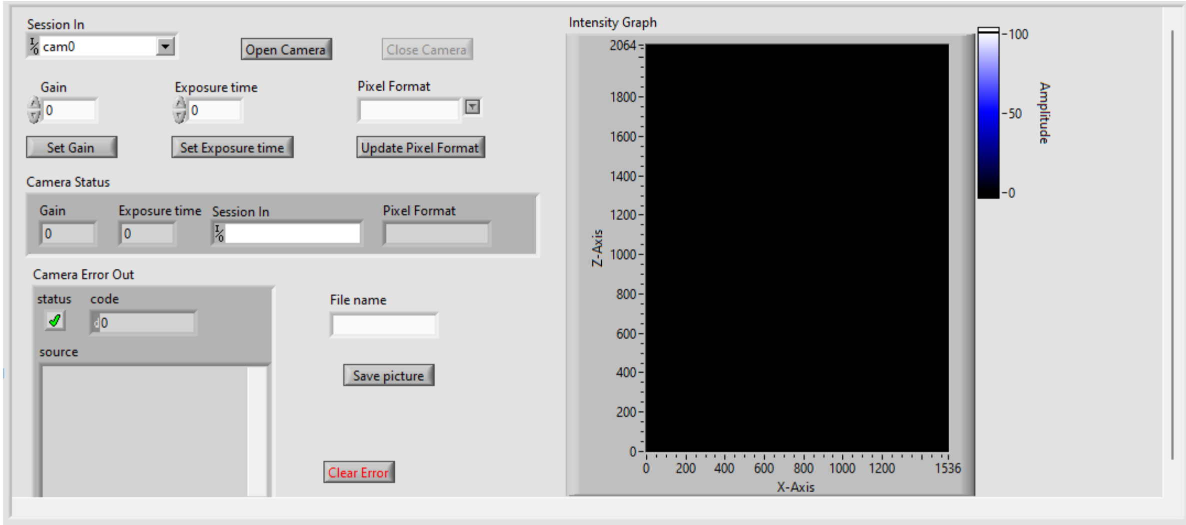

Figure 18: Picture of the front panel of the *Camera Control* actor. While to the left the controls to establish the connection to the camera and to change the acquisition parameters are visible, the last recorded image is shown on the right side.

The fourth device steering actor, the *Laser Controller* actor, communicates with the Teensy 4.1 and the program it executes, the laser control software, which is described in the previous section (3.2.1). The connection is established via an USB cable. For that, the corresponding port has to be selected in the front panel of the actor (see figure 19) and the *Open* button pressed. Thereafter, the *Laser Controller* receives the updated status of the laser and its current mode every second. The receipt of the message triggers two processes. On the one hand, the status of the LEDs on the front panel, which resemble the ones on the pinboard, as well as the switches labeled *ReadyToShoot* and *ManualEnable* are updated. On the other hand, the status and mode in the *Messages* box in the top right corner are refreshed. With the controls in the lower area on the left side messages can be sent to the Teensy 4.1. The *Laser(Continuous Pulses)* switch sends the commands laser on (1) and off (0) if its state is changed. With the button *Single Shot*, the message for a single laser pulse (2) is sent. Changing the average power in continuous pulses mode is achieved by the adjusting the control labeled *ppm Power for Continuous Pulses Mode* and pressing the button *Set ppm*, which then triggers the command 3 with the desired fraction attached. Lastly, the duration of a single pulse can be set by typing the requested value into the control box labeled *Singe Shot Pulse Duration in* μs and pressing the *Set Duration* button. By this the message 4 is forwarded, together with the data specifying the duration. As explained above, every time the Teensy 4.1 receives a message, this is reassured by sending the same message back and expressing the subsequently performed action together with a timestamp. Upon receipt of these messages by the *Laser Controller* actor, they are displayed in the corresponding lines in the top right *Messages* box.

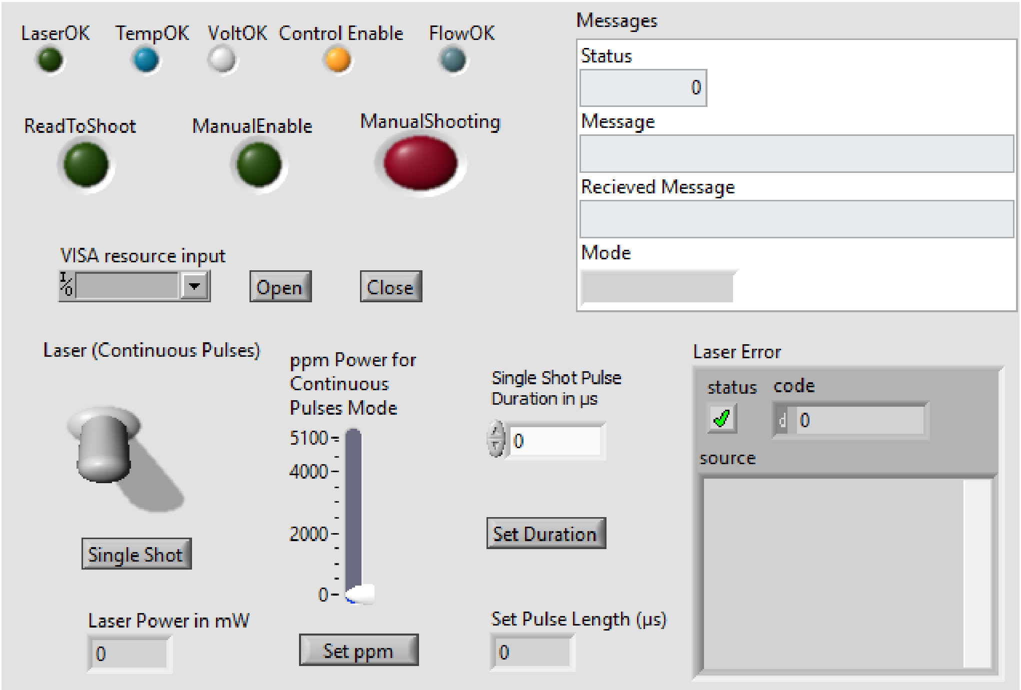

Figure 19: Picture of the front panel of the *Laser Controller* actor. In the left top area, the status LEDs and switches are depicted. In the messages box in the top right corner, all messages sent and received from the Teensy 4.1 are shown. With the controls in the lower section, the operating parameters are set and the laser operated.

4 Fiber production

In this section, the fabrication process of the fibers for FFPCs is discussed in detail. The production starts with the optical fiber, which is cleaved to pieces of the desired length and positioned in the fiber holder. Before the shooting can take place, the setup has to be calibrated by measuring the beam shape of the CO_2 laser in the vicinity of the focal point and thereby determining the position of the waist w_0. When these parameters have been identified, the fiber holder is mounted to the 3-axis motorized stage and the fiber tip brought to the required position. Then, the surface is ablated by the CO_2 laser beam and a depression created. Afterwards, the fiber tip is moved to the focal point of the Mirau interferometer and the shape of its surface is measured. If necessary, the geometry can be modified by additional pulses, until, in an iterative fashion, the desired form is obtained. Subsequently, the fibers are sent to an external company, where a high reflective coating is applied. Thereafter, the fibers are ready to be tested and used to build a FFPC.

4.1 Shooting procedure

Prior to firing with the CO_2 laser onto the fiber tips, the shape of the beam behind the ZnSe focal lens, in the vicinity of the waist w_0, has to be determined. Since for light with a wavelength of $9.3\,\mu\mathrm{m}$ no camera exists, the method of taking images at various positions and using the intensity distribution to determine the corresponding beam size is not available here. Instead, the so-called knife edge test is used. This method works as follows: An object with a pointed and straight brink, for example a razor blade, is mounted to the 3-axis motorized stage and moved step-wise perpendicular to the laser beam. While at first the full intensity of the beam reaches the power meter, the measured value decreases gradually as the knife advances. Since the beam exhibits a Gaussian profile and the power meter records the sum over the whole area, the obtained signal resembles a mirrored error function, as it is the integral of the Gaussian distribution. Via fitting an error function to the data the width of the beam can be deduced. This is done in vertical as well as horizontal direction and repeated for various positions along the path of the beam (denoted as axis Y). Combining the measurements yield the global parameters of the Gaussian beam as depicted by figure 4, namely the waist w_0 and the Rayleigh length z_0. Figure 20 shows the mask of the *Controller* actor, where all measurement parameters for the knife edge test have to be set. The data for horizontal (YX) and vertical (YZ) direction is recorded separately. For the respective measurement, the number of steps as well as their sizes in both directions, the waiting time between a step and a measurement as well as the number of data points per location have to be specified. If more than one measurement per position is chosen, the average of all recorded powers is used as the value of the corresponding site. The measurement begins by pressing the respective *start* button. Prior to that, the power meter has to be connected and set to zero, the laser has to be in continuous pulse mode and the razor blade brought to the desired starting position. With the *stop* button, the knife edge test can be terminated at any time. By clicking on the fourth button, the plots of the recorded data and the results of the fits are shown.

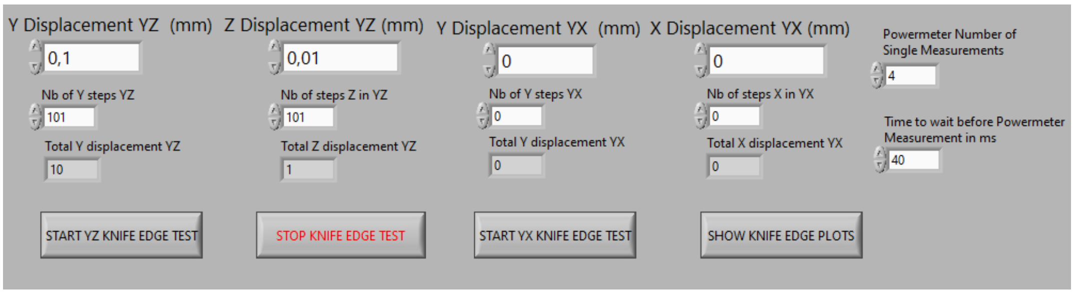

Figure 20: Picture of the knife edge test control panel. For either the test in horizontal (YX) or vertical (YZ) direction, the step-sizes as well as numbers in both ways, the time delay between a step and a measurement as well as the number of measurements per position (over which the average is taken), have to be specified. The buttons either start or stop the test or display the results.

Figure 21 depicts the measured beam shape along the propagation axis Y. The outliers at $y = -5.5\,\mathrm{mm}$ and $y = -0.4\,\mathrm{mm}$ are caused by large fluctuations of the measured power values in the central region of the beam. To improve the measurement, the waiting time can be extended, the number of single measurements per position can be increased and the step-size can be diminished. The measurement was performed with the parameters given in figure 20. While the knife edge test is capable of determining the shape of the beam and the position of the waist w_0 in longitudinal (Y-) direction precise enough, its lateral (X and Z) location has to be determined with higher precision.

For this task the following approach is chosen. A glass plate is mounted to the stages and punctuated by the CO_2 laser at different distances close to the position of the waist w_0. With the interferometric method presented in section 4.2, the size of each hole can be determined. The closer the depression was created to the position of the waist w_0, the smaller it is, meaning that the tiniest one was produced nearest to the smallest cross section of the laser beam. However, it is not settled whether the desired surface geometry is ablated when the fiber tip is exactly at the position of the waist w_0 in lateral direction. By repeating this procedure the position for creating the optimal depressions can be found. This approach also yields the relative distance between the best ablation location and the focal point of the Mirau interferometer with an accuracy well below $1\,\mu\mathrm{m}$ in lateral direction. This information is crucial for the following shooting procedure. To allow efficient coupling of light from the fiber mode to the cavity mode, the core needs to be as close to the center of the mirror as possible. Therefore, the fiber in the holder is at first brought to the interferometry section of the setup and its center positioned at the focal point of the Mirau objective. From there the tip is transferred by the previously determined relative distance to the designated fabrication location. Subsequently, the fiber tip is ablated by a single pulse or a series of shots.

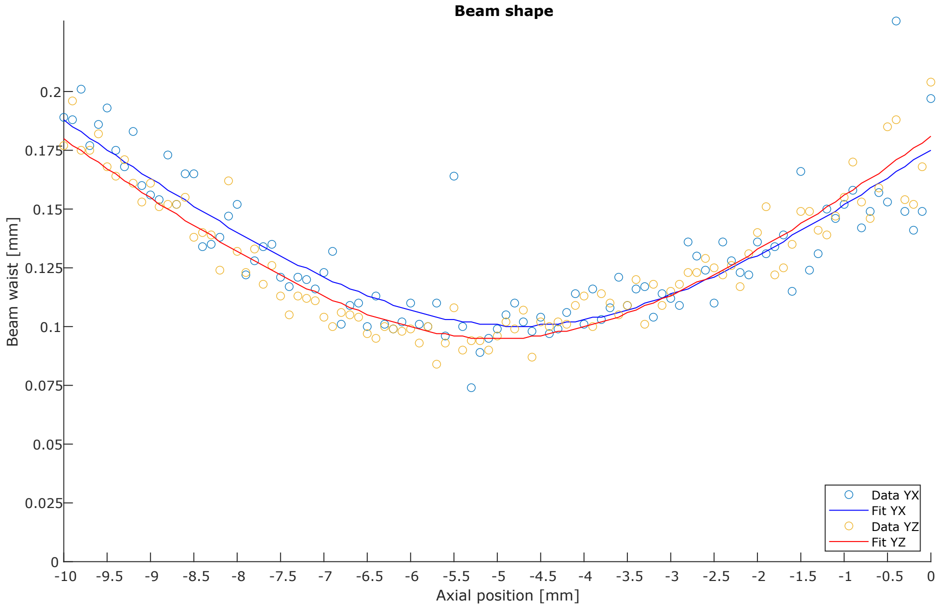

Figure 21: Picture of the beam shape in the vicinity of the waist. The circles represent the fitted beam waists and the continuous lines the fit of the Gaussian fundamental mode to the circles. The plots in blue belong to the measurements in horizontal direction and the ones in red to those performed vertically. Here, the measured waist is about 100 µm and the Rayleigh length approximately 3 mm.

4.2 Surface analysis

To reconstruct the shape of a depression created with the CO_2 laser, two steps are necessary. At first, an interferometric measurement is performed using the interferometer part of the setup described in section 3.1.2. Subsequently, the data is evaluated with *MATLAB*. For the measurement, the light from the LED traverses the NPBS, is focused by the Mirau objective and split by its semitransparent window. One part is reflected to the internal reference mirror and the other part is transmitted to the sample. After the reflection at the reference mirror and the surface of the sample, both beams interfere. The generated interferogram is then projected onto the camera. Due to a short coherence length of about 2 µm of the used light, the oscillations are localized around a prominent peak in the intensity signal, at which a region is at optical contact. This means that the distances between the window of the Mirau objective and this region respectively the reference mirror are equal. The sample is moved step-wise (with a step size of 10 nm to 20 nm) along the direction of the beam and at each position an image is taken. The required total range depends on the depth of the depression and has to cover the full interference features of both the lowest and the highest point. Typically, this corresponds to a distance of 4 µm to 8 µm.

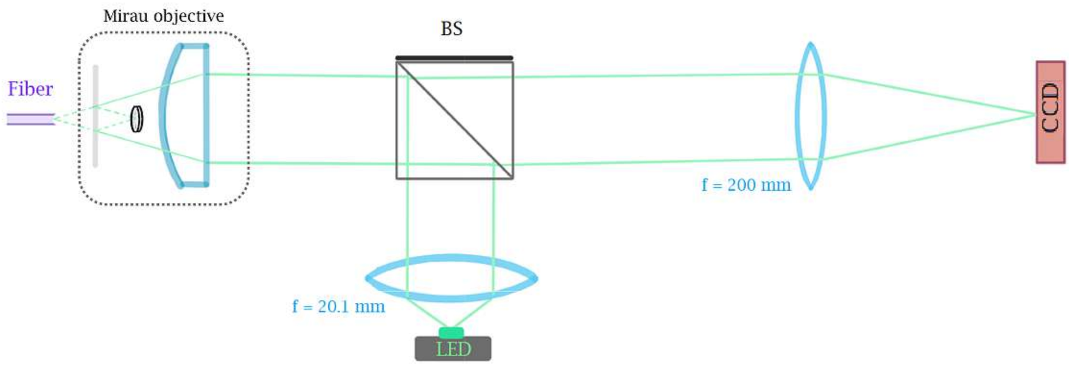

Figure 22: Sketch of the interferometric measurement. The light from the LED traverses the NPBS and is focused by the Mirau objective. One part of the light is reflected by its semitransparent window to the internal reference mirror and the other part transmitted to the sample. After the light has been reflected by the reference mirror and the sample, the beams from the two paths interfere and their interferogram is projected onto the camera. Due to the short coherence length of the used light, there is a distinguished peak in the intensity if a region is at optical contact, meaning that its distance from the window of the Mirau objective is the same as the distance from the reference mirror to the window. For the measurement, the sample is moved step-wise (with a step size of $10\,\mathrm{nm}$ to $20\,\mathrm{nm}$) along the direction of the beam and at each position an image is taken. Sketch adapted from [21]

An example for the recorded data of a single pixel on the camera is shown in figure 23. Its shape can be described as a sinusoidal signal with a Gaussian envelope, whose peak is at the position of optical contact. The goal of the data analysis algorithm is to determine this location precisely. In principle it is possible to fit the exact function to the data for each pixel as shown in figure 23.

However, this approach is computationally expensive and takes over an hour per fiber tip. Thus, it is rather impractical when the shapes of dozens of fibers have to be analyzed. Hence, this method is only used for a few pixels (for a few thousands out of several hundred thousand pixels), which takes less than a minute, to obtain a good estimate for the frequency of the sinusoidal component of the measured signal. This frequency f is directly linked to the spectrum of the LED light and the step-size Δs via the relation $f = \frac{2\pi\Delta s}{\lambda_{eff/2}}$. Here λ_{eff} denotes the effective center wavelength of the light source. The factor 2π arises from the conversion from frequency to angular frequency and the factor $1/2$ considers the fact that by moving the sample by half the wavelength the path of the light is changed by the full wavelength as it moves back and forth. The measured effective frequency was about $600\,\mathrm{nm}$, which is noticeable above the peak frequency of $554\,\mathrm{nm}$ given in the data sheet. Since the spectrum is asymmetric with larger wavelengths contributing more, the direction of the deviation is not surprising. But since the number of measurements was small, it cannot be stated whether the extent of the deviation is representative. The frequency is then used to determine the relative phases of all pixels. Since all other parameters such as frequency and amplitude are fixed, the determination of the only remaining free parameter - the phase in which we are interested - is much faster and takes about two minutes per fiber. This is done by computing the product of the measured data and the fit function for different phases and searching for the maximum of this quantity. Additionally, this procedure is more accurate than simple algorithms like the brightest pixel method [3], which uses only the information regarding the point where the highest intensity was measured [22]. The method applied here is quite robust against noise since it relies on the phase information of multiple sine oscillations. The phase-fitted sine function is exemplary depicted by figure 24.

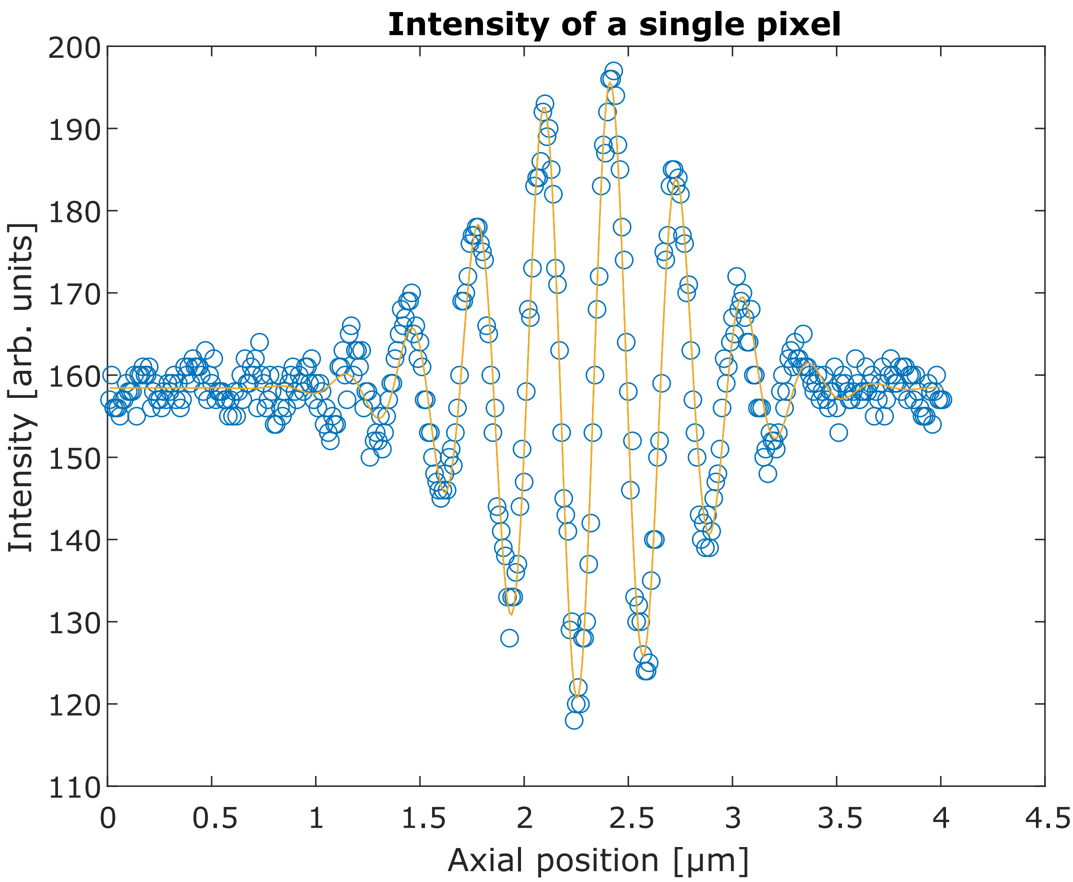

Figure 23: Graph of a single measurement including a fit. The blue dots represent the data and the continuous line the fitted Gaussian enveloped sine function.

After the relative phases (up to a factor of 2π) have been obtained, the phases are unwrapped and the geometry is rescaled. For this task the phase unwrapping algorithm presented in [23] is used. Figure 25 shows the wrapped phases as well as the reconstructed shape.

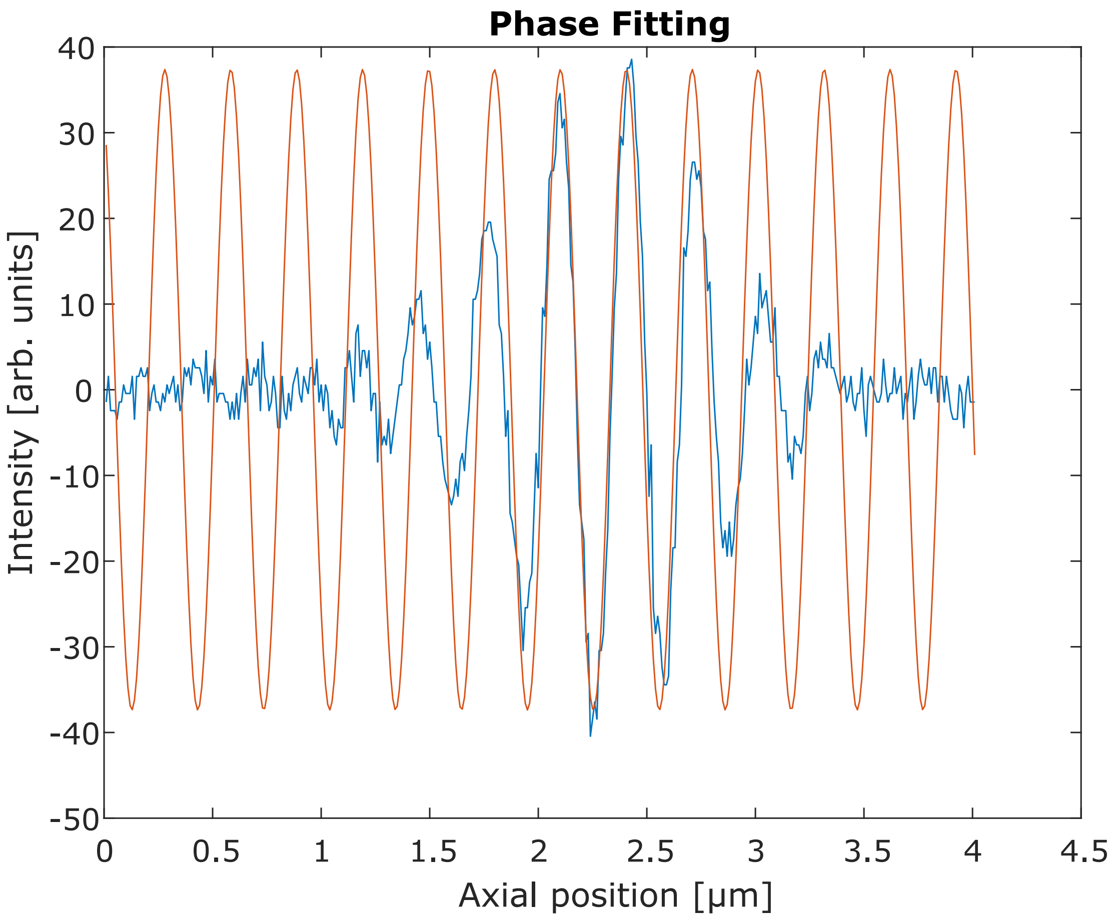

Figure 24: Graph of the phase fitted sine function. The blue line represent the data and the orange one the fitted sine function. From the intensity data the mean value was subtracted to obtain oscillations around zero.

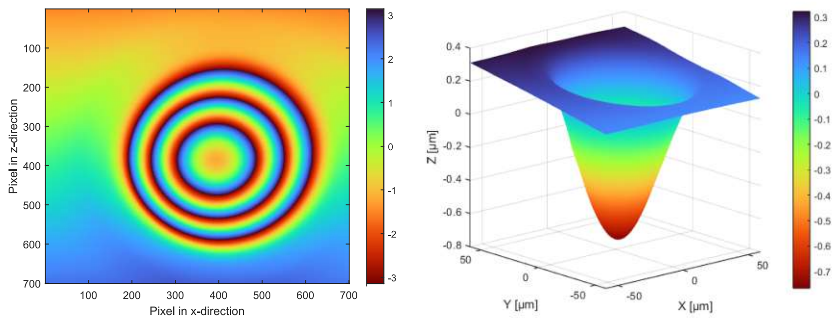

Figure 25: Graph of the wrapped phase and the reconstructed surface.

Once the surface has been reconstructed, a Gaussian function and a parabola are fitted to the central region. This yields an estimate for the radius of curvature as well as for the size of the future mirror. While for the radius estimation the inverse of the second derivative of the fit function at the apex is used, for the latter a deviation criterion is the determining factor. Figure 26 shows the fitted functions in horizontal and vertical direction on top of the data as well as the locations of these cross sections in the contour map. The depression whose interferometric data is used for all exemplary figures in this section was fabricated with a single $25\,\mu s$ CO_2 laser pulse. The created feature has a radius of curvature of approximately $500\,\mu m$ and a size of roughly $22\,\mu m$. For this first estimation of the mirror size a coarse criterion has been used: The size of the mirror is defined as the extension of the region, inside which the deviation of the fit from the data is smaller than $2\,nm$.

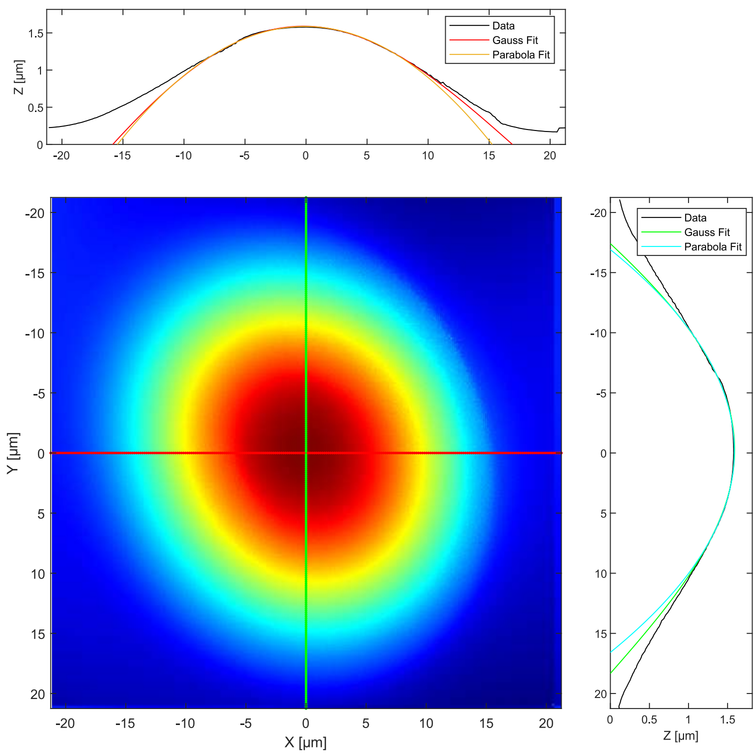

Figure 26: Graph of the reconstructed surface and the fitted functions. In the big section the location of the cross sections are indicated in the contour map of the reconstructed surface. The right and upper section show the data of the reconstructed surface together with the Gaussian and parabolic fits.

4.3 Coating

The high reflective coating necessary to achieve a high finesse (see formula 2) is applied externally by the company *Laseroptik*. For a finesse of $\mathcal{F} = 100\,000$ a reflectivity of roughly $R = 99.997\%$ is necessary. To reach that value, a series of thin layers with a thickness of about a quarter of the wavelength is applied to the surface using ion beam sputtering (IBS). The alternating layers consist of SiO_2 with a refractive index of $n = 1.58$ and Ta_2O_5 with $n = 2.09$. This configuration leads to constructive interference of the multiple reflected rays and almost perfect extinction of the transmitted light. The fibers are mounted in the upper part of a vacuum chamber used for this process, with their tips facing downwards. For that, the holders to which the fibers are loaded for the shooting process, are piled to stacks of eleven and screwed to a disk (see figure 27) which is then attached to a spindle in the chamber.

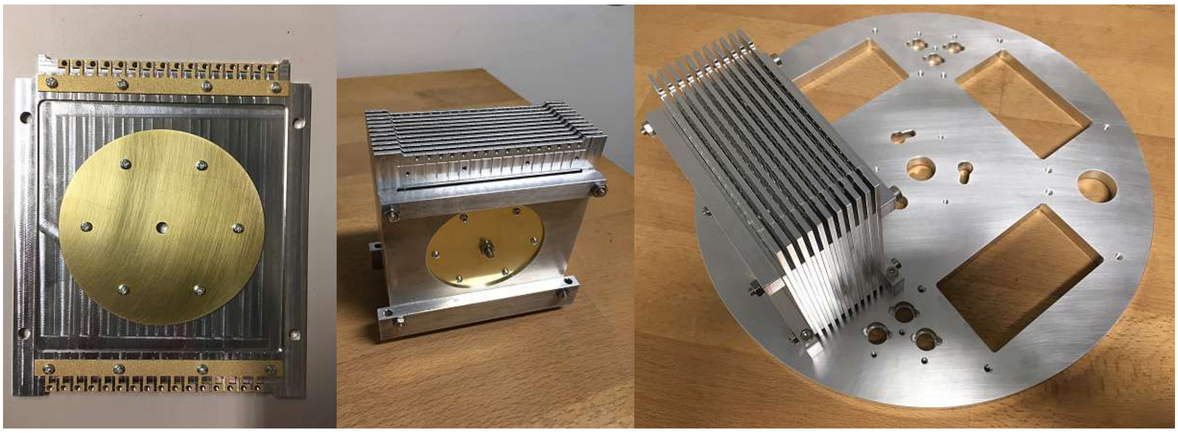

Figure 27: Picture of the fiber holder. In the left picture a single holder plate is shown, to which 16 fibers can be mounted. They are fixed at both ends with brass clamps and wound around the circle in the middle. The picture in the middle shows a pile of 11 holder plates stacked together. To the right one out of four possible stacks is mounted to the disk. The additional holes in the disk are for reference samples and the transmission measurement.

During the coating process the whole piece turns with a rotation velocity of $rpm = 120\,\mathrm{Hz}$ to produce layers of equal thickness over all fibers. To monitor the process, the transmission of a reference sample is measured in situ. The whole fiber holder was designed and manufactured in the course of this thesis with a couple of design goals. Based upon existing holders, the main ideas of our design were to facilitate the handling, to reduce the likelihood of errors and to provide space for a large number of fibers. The first two goals are mostly dealt with by the layout of the holder plate. The two brass clamping sheets at the edges allow to fix the ends of each fiber individually, facilitating to precisely position one fiber after another. The circle in the middle has a diameter of $3\,\mathrm{cm}$, which corresponds to the long term bending radius of the used fibers. Therefore, by winding the fibers around the circle, it is guaranteed that they do not break. Another advantage of this design is that the whole fibers are enclosed inside the fiber plate, which is separated from the next one in the stack by a distance plate. Hence, there are no loose fiber tails that have to be fixed in the vacuum chamber and tied properly so that they stay in place while the spindle rotates during the coating process. Moreover, a single plate can be removed from a stack with no need to disentangle the fibers, a deliberate process during which they can break. With 16 fibers fitting onto a holder plate, 11 plates forming a stack and room for 4 stacks in the base plate, a maximum of 704 fibers can be coated in one run. This property does not only lead to low costs per coated fiber, but also increases the probability to receive fibers with the desired characteristics. One the one hand, this is beneficial in the phase of prototype production, since it has to be considered that at the beginning the success rate can be rather low and by this the chance to produce at least some fibers with favored properties is higher. On the other hand, the large number of fibers that can be coated simultaneously allows to reduce the number of necessary coating runs in the future and enables to produce a long lasting stock of fibers. Apart from providing space for many fibers to be coated, the disk also protects the fiber tips to some extend. By design the tips are located $1\,\mathrm{mm}$ above the base of the disk, so that the disk can be safely placed on a clean table with almost no risk of scratching a tip. Moreover, the disk provides the possibility for six half-inch glass plates to be coated as reference or test samples. After the coating process, the fibers are ready to use.

5 Outlook

This thesis deals with the fabrication of fiber mirrors for FFPCs. During its development, the experimental setup was fine tuned and the majority of the control as well as of the analysis software developed. Furthermore, many preparatory tasks for the production were conducted, especially the conception of the routine for the knife edge test, the design of the procedure to find the desired shooting parameters and of the method to obtain the relative distance between the focal point of the Mirau objective and the waist of the focused laser beam. Moreover, the algorithm to measure and reconstruct the ablated surface was developed and implemented. Additionally, investigations regarding the coating process were performed, resulting inter alia in the machining of the ready-to-use fiber holder.

Altogether, the whole setup has currently arrived at a stage close to the start of the prototype production. One of the next steps will be to integrate an AOM into the setup. By this, the laser power can be stabilized with a feedback loop, which will be a huge advantage compared to the present situation where only pulses with the full laser power can be applied. Besides, the obtained control over the precise pulse shapes is expected to improve the reproducibility of the produced depressions. Another subsequent step is to find the desired shooting parameters, at first on a flat glass plate and then on a fiber tip. Furthermore, the routine for the interferometric measurement can be automatized to facilitate the production of a large number of fibers.

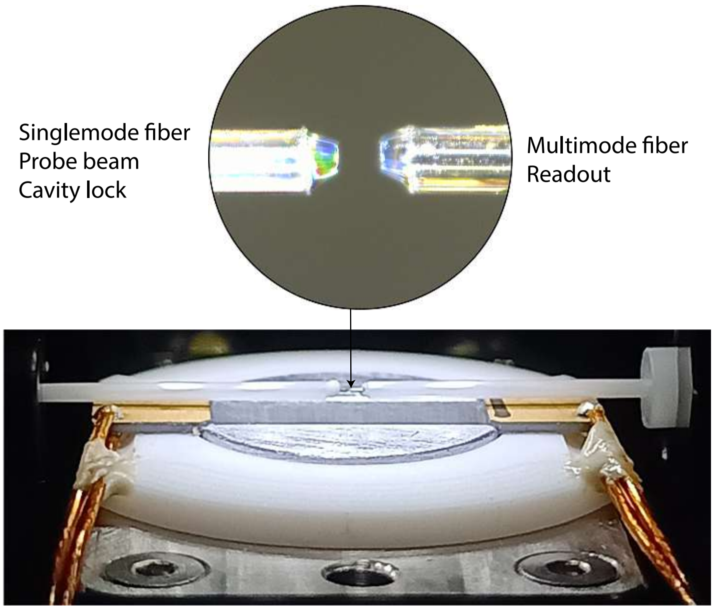

Figure 28: Picture of the current cavity. While in the lower section the whole assembly with the fibers in the ferrules which are glued to the piezos who in turn are glued to the white MACOR piece is shown, the detail displays the fiber mirrors that form the cavity.

All in all, this fabrication process promises to yield fibers with a finesse over $100\,000$ and mirror sizes of some $10\,\mu m$. This would be major improvement compared to the currently used mirrors with finesses of $30\,000$ to $50\,000$ and an usable size of approximately $15\,\mu m$. These properties let the current FFPC, as depicted by figure 28, reach a cooperativity of roughly $C = 80$ at a length of $80\,\mu m$, which drops significantly with increasing cavity size. With our new mirror fabrication setup we hope to reach cooperativities above 100 at lengths between $150\,\mu m$ and $250\,\mu m$. This would give rise to the possibility of loading more than 100 atoms to the cavity, enabling to access new realms of physics experimentally.

References

[1] David Hunger et al. “A Fiber Fabry-Perot cavity with high finesse”. In: *New Journal of Physics* 12 (2010), p. 065014. DOI: 10.1088/1367-2630/12/6/065038.

[2] Eugene Hecht. *Optics*. 5th edition. Pearson, 2017. ISBN: 978-0-13-397722-6.

[3] Michael Kubista. “A New Fiber Mirror Production Setup”. Master Thesis. Bonn: Rheinische Friedrich-Wilhelms-Universität Bonn, 2017.

[4] Wolfgang Demtröder. *Experimentalphysik 2*. 7th ed. Vol. 2. Heidelberg: Springer, 2017. ISBN: 978-3-662-55789-1.

[5] Nur Ismail et al. “Fabry-Pérot resonator: spectral line shapes, generic and related Airy distributions, linewidths, finesses, and performance at low or frequency-dependent reflectivity”. In: *Optics Express* 24 (2016), pp. 16366–16389. DOI: 10.1364/OE.24.016366.

[6] Hannes Pfeifer et al. “Achievements and Perspectives of Optical Fiber Fabry-Perot Cavities”. In: *Applied Physics B* 128 (2022), p. 29. DOI: 10.1007/s00340-022-07752-8.

[7] Manuel Uphoff. “Optical microcavities for quantum communication with single atoms”. Doctoral Thesis. Technische Universität München, 2017.

[8] Julian Léonard. “A Supersolid of Matter and Light”. Doctoral Thesis. ETH Zurich, 2017. DOI: 10.3929/ethz-b-000262194.

[9] Dieter Meschede. *Optik, Licht und Laser*. 3rd edition. Studium. Wiesbaden: Vieweg + Teubner, 2008. ISBN: 978-3-8351-0143-2.

[10] Igor Dotsenko. “Single atoms on demand for cavity QED experiments”. Doctoral Thesis. Bonn: Rheinische Friedrich-Wilhelms-Universität Bonn, 2007. URL: https://nbn-resolving.org/urn:nbn:de:hbz:5N-10697.

[11] Bahaa Saleh and Malvin Teich. *Fundamentals of Photonics*. 3rd edition. Vol. 2. John Wiley & Sons, 2019. ISBN: 978-1-119-50687-4.

[12] Natalie Thau. “Optical fiber cavities”. Master Thesis. Bonn: Rheinische Friedrich-Wilhelms-Universität Bonn, 2012. URL: http://quantum-technologies.iap.uni-bonn.de/de/diplom-theses.html?task=download&file=259&token=14767896a5f142a74d35dae9fb8e2804.

[13] Rei Kitamura, Laurent Pilon, and Jonasz Miroslaw. “Optical constants of silica glass from extreme ultraviolet to far infrared at near room temperature”. In: *Applied Optics* 46 (2007), pp. 8118–8133. DOI: 10.1364/AO.46.008118.

[14] Steven Yang et al. “Comparing the use of mid-infrared versus far-infrared lasers for mitigating damage growth on fused silica”. In: *Applied Optics* 49 (2010), pp. 2606–2616. DOI: 10.1364/AO.49.002606.

[15] Christian Deutsch. “High Finesse Fibre Fabry-Perot Resonators - Production, Characterization, and Applications”. Doctoral Thesis. LMU München, 2008. URL: `https://hdl.handle.net/11858/00-001M-0000-000F-B4D5-B`.

[16] David Hunger et al. *Laser micro-fabrication of concave, low-roughness features in silica.* 2011. DOI: `10.48550/arXiv.1109.5047`.

[17] Anthony McLachlan and Fred Meyer. “Temperature dependence of the extinction coefficient of fused silica for CO_2 laser wavelengths”. In: *Applied Optics* 26 (1987), pp. 1728–1731. DOI: `10.1364/AO.26.001728`.

[18] Daniel Najer et al. “Fabrication of mirror templates in silica with micron-sized radii of curvature”. In: *Applied Physics Letters* 110 (2017), p. 011101. DOI: `10.1063/1.4973458`.

[19] Johannes Schabbauer. “Experiment control for quantum simulation with non-local interactions”. Master Thesis. Wien, 2023. DOI: `10.34726/hss.2023.104001`.

[20] Andreas Reiserer and Gerhard Rempe. “Cavity based quantum networks with single atoms and optical photons”. In: *Reviews of Modern Physics* 87 (2015), pp. 1379–1418. DOI: `10.1103/RevModPhys.87.1379`.

[21] Isabelle Safa. “Fiber Fabry-Perot Cavity for enhanced atom-light interactions”. Master Thesis. Vienna: TU Wien, 2023.

[22] Dongxu Wu and Fengzhou Fang. “Development of surface reconstruction algorithms for optical interferometric measurement”. In: *Frontiers of Mechanical Engineering* 16.1 (Mar. 1, 2021), pp. 1–31. ISSN: 2095-0241. DOI: `10.1007/s11465-020-0602-6`.

[23] Miguel Arevallilo Herráez et al. “Fast two-dimensional phase-unwrapping algorithm based on sorting by reliability following a noncontinuous path”. In: *Applied Optics* 41 (Dec. 10, 2002), pp. 7437–7444. DOI: `10.1364/AO.41.007437`.

Acronyms

AOM acousto-optical modulator.

CMOS complementary metal oxide semiconductor.

CQED cavity quantum electrodynamics.

FFPC Fiber Fabry Perot cavity.

FPI Fabry-Perot interferometer.

FWHM full width at half maximum.

HWHM half width at half maximum.

IBS ion beam sputtering.

IMAQ image acquisition.

LED light emitting diode.

NPBS non polarizing beam splitter.

PWM pulse-width modulation.

QWP quarter-wave plate.

USB universal serial bus.

VISA virtual instrument software architecture.

List of Figures